UNIVERSIDADE D
COIMBRA

Pedro Jaime Luís Soares

COMPORTAMENTO MECÂNICO E TRIBOLÓGICO DE PEÇAS 3D FABRICADAS POR PROCESSOS ADITIVOS

VOLUME 1

Dissertação no âmbito do Mestrado em Engenharia Mecânica na Especialidade de Produção e Projeto orientada pela Professora Doutora Ana Sofia Figueira Ramos e pela Professora Doutora Maria Teresa Freire Vieira e apresentada ao Departamento de Engenharia Mecânica da Faculdade de Ciências e Tecnologia da Universidade de Coimbra

Setembro de 2022

1 2 9 0

FACULDADE DE CIÊNCIAS E TECNOLOGIA
UNIVERSIDADE D COIMBRA

Mechanical and Tribological Behaviour of 3D Parts Manufactured by Additive Processes

Submitted in Partial Fulfilment of the Requirements for the Degree of Master in Mechanical Engineering in the speciality of Production and Project

Comportamento Mecânico e Tribológico de Peças 3D Fabricadas por Processos Aditivos

Author

Pedro Jaime Luís Soares

Advisors

Ana Sofia Figueira Ramos

Maria Teresa Freire Vieira

Jury

President	**Professor Doutor Diogo Mariano Simões Neto** **Professor Auxiliar da Universidade de Coimbra**
Vowel	**Doutor Luís Miguel Cardoso Vilhena Pereira da Silva** **Investigador da Universidade de Coimbra**
Advisor	**Professora Doutora Maria Teresa Freire Vieira** **Professora Catedrática Convidada da Universidade de Coimbra**

Coimbra, September 2022

“Concentrate all your thoughts upon the work at hand. The sun's rays do not burn until brought to a focus.”

Alexander Graham Bell

ACKNOWLEDGEMENTS

The work here presented would never be possible without the collaboration and support of some people who I praise below:

I would like to thank Professor Teresa Vieira for allowing me to work on such an interesting and challenging theme and for all the wisdom shared.

To thank Professor Sofia Ramos for all the guidance, dedication, concern, availability to help, and scientific knowledge sharing.

To thank Professor Amilcar Ramalho for the scientific discussions.

To thank Professor Luís Vilhena for the guidance during microabrasion tests.

To thank Daniel Gatões for all his guidance, patience, clear explanations, and enormous help with microtomography images.

To thank Luís Cacho for allowing me to observe his shaping MEX steps, for all the explanations, and 3D printing advices.

To thank Bernardo Alves, especially for his help with the debinding and sintering steps of MEX.

To thank Francisco Cruz for always being ready to help and share scientific knowledge.

I would like to thank Tomás Resendes for teaching me polishing and Gonçalo Oliveira for all the useful advice.

To thank Marcionilo Neri for the perfectly polished specimens.

I would also like to thank my research laboratory colleagues Cristina, Rafael, Patricia, Akel, Micaela, Catarina, and Pedro for all the relaxing moments.

Last but not least I want to leave a word of respect and gratitude to my parents Jaime and Céu, my brother Emanuel, and Beatriz, and my university and life friends João and Pedro for always encouraging and supporting me.

Abstract

Additive manufacturing (AM) technologies allow to produce parts/systems/devices with geometries not possible by subtractive and formative processes. Moreover, it should be noted that AM processes use powder particles as raw material.

The present study is based on understanding the influence of thickness on the quality of the 3D object using an indirect additive manufacturing, denominated Material Extrusion (MEX). Microtomography was essential to improve the evaluation of defects inside the 3D objects as green and sintered. Green specimens with different thicknesses (3 and 5 mm) were successfully printed using a filament made from a feedstock with 60%vol. of 316L stainless steel powder and 40%vol. of organic binder and additives, according to previous optimization. Nevertheless, after debinding and sintering under an argon atmosphere only the specimens with the lower thickness (3 mm) had engineering quality. The specimen with 5 mm thickness presented cracks after debinding and sintering, mainly due to the impossibility of degassing the organic constituents of the feedstock during debinding. After consolidation (sintering), some mechanical properties such as hardness and Young's modulus of 316L stainless steel were evaluated. An approach to the microabrasive wear resistance behaviour of the 3D objects produced by MEX was evaluated using a ball-cratering apparatus.

This study shows that MEX can be a valid alternative to manufacture 316L stainless steel 3D objects but with thicknesses up to 3 mm. For higher thicknesses, new designs with inside channels to favour degassing must be considered.

Keywords: MEX, 316L (AISI), Defects, Microabrasion, Microtomography (μCT), Thickness of 3D objects.

Resumo

As tecnologias de fabrico aditivo permitem produzir peças, sistemas e dispositivos com geometrias impossíveis de obter por processos convencionais. Os processos aditivos utilizam partículas de pó como material base.

O estudo apresentado visa a compreensão da influência da espessura na qualidade do objeto 3D, obtido por um processo aditivo indireto, denominado MEX – Extrusão de material. A microtomografia foi essencial para melhorar a avaliação dos defeitos no interior dos objetos 3D, quer em verde, quer sinterizados. Diferentes geometrias de provetes de espessuras diferentes (3 e 5 mm) (verdes) foram impressas com sucesso, recorrendo ao mesmo tipo de filamento proveniente de uma mistura previamente otimizada, que continha 60% em volume de pó de aço inoxidável 316L e 40% em volume de ligante e aditivos orgânicos. A eliminação do ligante e aditivos, e a sinterização foram realizadas em atmosfera de árgon. Apenas os provetes com 3 mm de espessura apresentaram a qualidade pretendida. Os provetes de 5 mm revelaram fissuração e separação em duas partes distintas, devido essencialmente à impossibilidade de desgaseificação dos gases resultantes da ustulação da parte orgânica do verde e retenção do árgon da atmosfera envolvente, durante a eliminação do ligante e aditivos (castanho). Após a consolidação (sinterização), as propriedades mecânicas do aço inoxidável 316L, dureza e o módulo de Young foram determinadas, assim como efetuada uma avaliação preliminar da resistência ao desgaste microabrasivo dos objetos 3D de espessura inicial de 3 mm produzidos por MEX.

O estudo fundamentalmente demonstra que o MEX pode ser uma alternativa válida para fabricar objetos 3D, se os mesmos não tiverem espessuras superiores a 3mm. Caso se pretenda ultrapassar essa espessura, será necessária a introdução de novos sistemas de exaustão, como por exemplo canais internos que promovam a desgaseificação.

Palavras-Chave: MEX, 316L (AISI), Defeitos, Microabrasão, Microtomografia, Espessura dos objetos 3D.

Contents

LIST OF FIGURES

LIST OF TABLES

LIST OF SYMBOLS AND ACRONYMS/ ABBREVIATIONS

List of Symbols

ρ – Density

ρ_{Wv} – Density when coated with varnish

m_{Wv} – Mass when coated with varnish

m_{SWv} – Mass when submerged and coated with varnish

k – Specific wear rate

L – Sliding distance

N - Normal load

V – Wear volume

Acronyms/Abbreviations

3D – Three Dimensional

AISI - American Iron and Steel Institute

AM - Additive Manufacturing

ASTM – American Society for Testing and Materials

BJT - Binder Jet Technology

CAD – Computed Aided Design

CIP – Cold Isostatic Pressure

CPVC – Critical Powder Volume Concentration

CT – Computed Tomography

DEM – Department of Mechanical Engineering

DMLS – Direct Metal Laser Sintering

DSCP – Direct Shell Production Casting

EDS – Energy Dispersive X-Ray Spectroscopy

FCTUC – Faculdade de Ciências e Tecnologia da Universidade de Coimbra

FDM – Fused Deposition Modelling

HMV – Micro Vickers Hardness

IFM – Infinite Focus Microscopy

ISO – International Organization for Standardization

LENS – Laser Engineered Net Shaping

LOM – Laminated Object Manufacturing

M1 – Master Binder

MEX – Material Extrusion Additive Manufacturing of Metal

MHV – Micro Hardness Vickers

MIM – Metal Injection Moulding

OM – Optical Microscopy

PIM – Powder Injection Moulding

PBF – Powder Bed Fusion

RPD – Rapid Plasma Deposition

SEM – Scanning Electron Microscopy

SDS – Shaping, Debinding and Sintering

SGC – Solid Ground Curing

SLS – Selective Laser Sintering

SLM – Selective Laser Melting

SS – Stainless Steel

STL – Standard Tessellation Language

TGA – Thermo Gravimetric Analysis

TPE – Thermoplastic Elastomer

UMHV – Ultra Micro Hardness Vickers

UTS – Ultimate Tensile Strength

WM – Wrought Manufactured Material

1. INTRODUCTION

Engineering is, undoubtedly, the fundamental pillar of human technological evolution, where knowledge and imagination are reflected. This craft is based on the ability to think about everyday needs and adversities and provide answers/explanations through the development of new products.

This dissertation results from the intensive work developed during the last semester of the Master in Mechanical Engineering, carried out at the Materials and Surface Engineering Laboratory of the Department of Mechanical Engineering (DEM), of the Faculty of Sciences and Technology, of the University of Coimbra (FCTUC).

Industry 4.0, also known as the 4th industrial revolution, is changing the way companies manage themselves. Especially manufacturers are integrating technologies such as machine learning and cloud computing in their facilities and production management. These smart facilities are equipped with proper hardware and software that continuously collects and processes data to improve decision-making, management, and production lines leading the companies to increase their visibility and consequently, their competitiveness [1].

Additive Manufacturing (AM) is increasingly an emerging theme in the field of metallic materials engineering, especially by its feasibility, cost, and time reduction capacity. Once AM is an enabling technology helping with new products, businesses, models, and supply chains, it has to inescapably be classified as a 4.0 Industry area, satisfying conditions such as data sharing, customization and complexity of 3D objects. In fact, AM technologies are particularly promising for producing parts/systems/devices, with external and internal geometries, not possible by other manufacturing processes, either subtractive or replicative. However, in opposition to conventional raw materials, usually in the form of bars, wires or sheets; additive manufacturing processes frequently use powder particles as raw material, introducing new challenges.

Porosity is unescapably associated with the powder concept. The porosity content depends on the powder, selected technology, parameters controlled during the process and

final application. A structural application demands exhaustive awareness of porosity and how it influences the mechanical properties of the 3D object obtained by AM.

In this context, the present work aims at evaluating the porosity, namely the content and distribution of pores, within 3D objects produced by Material Extrusion (MEX), and analysing its influence on the mechanical and tribological (microabrasion) behaviour. MEX was the selected AM process due to its simplicity and equipment low cost, as well as due to the know-how and competencies existent at DEM/FCTUC.

In order to contribute to maximize the performance of functional and structural 3D objects made by MEX, this research work comprises different stages of the MEX process for 316L stainless steel powder.

Production of feedstock, 3D printing, debinding and sintering will be the main steps of this indirect additive manufacturing process. The role of the 3D object thicknesses in the final quality of 3D objects will be emphasized. Optical (OM) and scanning electron microscopies (SEM), and microtomography (μCT) are the main characterization techniques. The μCT is particularly relevant as it is a powerful non-destructive testing tool that allows the voids and pores (> 10 μm) inside the 3D objects to be analysed. The mechanical behaviour (hardness and Young's modulus) was evaluated by depth sensing indentation, and abrasive wear testing of the 3D objects by ball-cratering was also carried out. The initial objective of this dissertation was to submit the 3D objects to cavitation-erosion tests. However, due to equipment failure cavitation tests were replaced with microabrasion tests (ball-cratering).

During the work skills associated with the production of feedstocks - bulk raw material supplied to the AM building process - (rheometer and extruder), 3D printing (Repetier and Prusa software and MK3s printer), debinding and sintering, polishing, OM, SEM, depth-sensing indentation, basics of μCT, and wear testing (cavitation and ball-cratering) were acquired.

The document is divided into 5 chapters, including this introduction followed by a state of art where a review is made that starts with the overall AM and then focuses on MEX, which is an indirect AM process. It also contains information about the 316L stainless steel, the base material for this work, and finally, a reference to abrasive wear testing is reported. Chapter 3 consists of the material selection, the outlined methodology, and a brief

explanation of the characterization techniques. In Chapter 4, the developed work is presented, and the results are discussed. Finally, in chapter 5, the main conclusions are exhibited, highlighting the most relevant results, and including suggestions for future work.

2. STATE OF ART

Additive Manufacturing was first introduced in the 1980s and ever since its grown never stopped. Nowadays, manufacturers from all branches of the industry either implemented or are implementing this competitive worldwide way of manufacturing. As an evolving theme, it is a very interesting area for researchers to study.

2.1. Additive Manufacturing

According to ISO/ASTM 52900:2021, AM is the "process of joining materials to make parts from 3D model data, usually layer upon layer, as opposed to subtractive manufacturing and formative manufacturing methodologies" * [2].

Some AM advantages and different types of AM processes where is possible to work with metals are presented in Table 2.1 and Table 2.2, respectively.

Table 2.1. AM advantages

AM Advantages	
Environmental Benefits	In some AM processes, there will be material only where it is required.
Lower Energy Consumption	Fewer resources and tools are needed, meaning energy savings associated with material extraction.
Support of Lattice Structures	Light-reinforced parts where not only strength but also light weight is desired are easy to create.
Customization	Freedom and design innovation are not held back by cost and time constraints related to conventional manufacturing processes.
Legacy Parts	Parts that were no longer manufactured are now subject to redesign.

* Additive Shaping consists in acquiring the shape by successive addition of material, Subtractive Shaping consists of acquiring the shape by selective remotion of material (e.g., Milling, Drilling, …), and Formative Shaping consists in acquiring the shape by application of pressure to a body of raw material (e.g., Injection Moulding).

Table 2.2. Types of Metal AM Processes

AM Processes		
DIRECT	PBF – Powder Bed Fusion	Powder particles deposited on a powder bed are melted.
	DED – Direct Energy Deposition	Materials are melted as they are deposited.
INDIRECT	MEX – Material Extrusion	Material is extruded through a nozzle.
	BJ – Binder Jetting	A liquid binding agent is dispensed on powder to form a 2D pattern on a layer.
	LOM – Laminated Object Manufacturing	Sheets of material are bonded to attain a final part.

AM processes can be classified as direct or indirect processes. Direct processes are those where shaping coincides with consolidation. Some examples are PBF and DED. On the other hand, indirect processes are those where conformation and consolidation are completely separated in time, such as MEX, BJ, and LOM.

2.2. MEX

Material Extrusion is an indirect AM process that is used due to its simplicity and low cost of the required equipment. According to ISO/ASTM 52900:2021, MEX is an "additive manufacturing process in which material is selectively dispensed through a nozzle or orifice" [2]. The metal extrusion process consists of SDS (Shaping, Debinding and Sintering). MEX technology consists of mixture (feedstock) optimization, layer-by-layer printing, debinding and finally sintering to create a consolidated metal part. Figure 2.1 summarizes MEX

technology using a filament feeding system.

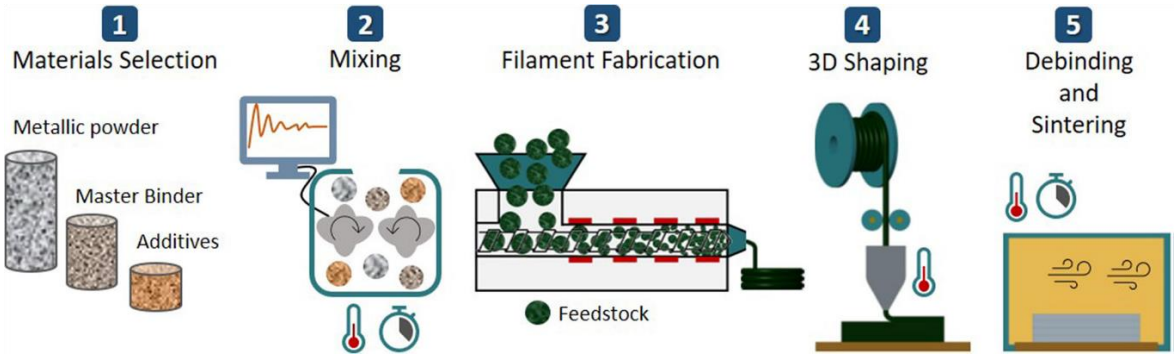

Figure 2.1. MEX technology **[3]**.

Three types of MEX can be considered depending on the feeding system of the printer (Table 2.3) [4]. The filament was the type selected in the context of this dissertation. Metal powder-based filaments have become more and more studied [3]–[7].

Table 2.3. MEX types function of feeding system.

	Filament	**Screw**	**Plunger**
Feedstock Type	Filament	Granulated	Bar/Granulated
Feeding Mechanism	Filament is softened by a heating element and extruded through a hardened nozzle	Continuous filling by a screw	Plunger pushes the feedstock through the nozzle
Metal Loading	Solid loading needs to consider stiffness and flexibility	CPVC* similar to MIM**	Solid loading is higher than filament-based
Pros	Low-cost equipment, simplicity and familiarity with 3D printing equipment (polymers)	Debinding and sintering similar to MIM green	No problems with feedstock flexibility
Cons	Necessity of filament production equipment and know-how.	Control of granulate size to obtain printing stability	Necessity of replenishing feedstock so printing discontinuity can occur
*CPVP – Critical Powder Volume Concentration **MIM – Metal Injection Moulding			

The first stage of the MEX process is shaping, which begins with material selection followed by mixing. The feedstock is then granulated, extruded in filament form and spooled depending on the printer type. Following, the filament is loaded into the printer, and the green part is obtained. According to the bibliography, there is a starting point to attain a successful extrusion – Table 2.4.

Table 2.4. Starting conditions for successful extrusion.

Starting Conditions
The materials selection phase is the 1st phase that influences the final results quality.
Powder concentration should be higher than 50%vol. but in a steady state (torque function of time).
Homogeneity in the powder-binder mixture must be attained.
The filament must achieve a suitable Stiffness-Flexibility behaviour.
Appropriate viscosity for printing.
Green part must be heat treated with a suitable thermal cycle.

2.2.1. Material selection

To guarantee a proper material selection powder must be characterized following the 4S's rule – Particle **S**ize, Particle **S**ize Distribution, Particle **S**hape, and **S**tructure. According to the state of art, the powder must have a spherical shape and narrow particle size distribution [8]. Particle size and size distribution can influence powder flowability (finer particles mean a higher free specific surface, thus friction between particles is increased, leading to higher torque, however, a higher free specific surface is required once one stage of the process is sintering). Moreover, surface topography (roughness) has also an important role in powder flowability. In terms of particle shape, the optimal one would be spherical (enhancing packing density allowing more powder to be added, and lowering shrinkage), resulting in a shape factor close to 1.

Binder and additives usually consist of the main binder (50-90%vol total binder), a backbone polymer (0-50%vol total binder), and additives (0-10%vol total binder) which can be dispersant agents, stabilizers, compatibilizers, etc [6]. Binder and additives' main objectives are to promote strength, stiffness, and flexibility of the green parts to assure successful debinding and sintering.

2.2.2. Feedstock

After selecting a suitable powder and binder system, the following step is creating a homogeneous biphasic mixture composed of powder and binder. Reaching homogenization of the mixture is very important since not only situations like powder agglomeration that contribute to feedstock brittleness must be avoided. In addition, if feedstock has a homogeneous powder distribution, printed parts will also have such distribution and, therefore, better quality is expected. The mixing temperature should be between binder softening and degradation temperature.

One of the challenges of MEX is to attain the highest possible green part density to achieve the best quality components and avoid excessive shrinkage. One way to reach the aforementioned goals is by finding the critical volume powder concentration (CPVC). Relevant studies, where torque measurements were used to evaluate CPVC, point to the occurrence of an abrupt increase of torque for contents higher than optimal powder volume [3], [9]. This is provoked by direct contact within particles which happens due to the unavailability of a binder to cover each metallic particle homogeneously. According to F.M. Barreiros and M.T. Vieira [9], the CPVC value corresponds to the last volume content of inorganic material before the torque variation becomes significant.

2.2.3. Extrusion

Once the feedstock is optimized, it is extruded in filament form. In opposition to PIM, flexibility plays a key role together with stiffness, once it should be easily handled, coiled, and extruded/printed [3].

According to the bibliography, optimal filament diameter is around $1.75 \pm 0.05\ mm$ [7], and deviations in filament diameter can be prevented by maintaining unchanged the distance between the extruder nozzle and working table. In Table 2.5 some problems due to the diameter variation are highlighted.

Table 2.5. Problems of unsuitable filament diameter.

Consequences of deviation in filament diameter	
$D_{feedstock} < D_{standard}$	There is insufficient flow, leading to insufficient layer height and width, which is associated with bad adhesion between consecutive layers and voids may also appear – Poor feed rate.
$D_{feedstock} > D_{standard}$	There will be excessive material in the printer channel. Hard extrusion is expected, and blocking may occur – Excessive feed rate.

2.2.4. Shaping

To attain the best quality of green parts and prevent phenomena like interlaying porosity, warpage, excessive shrinking, etc., it is important to use adequate shaping parameters.

Some key shaping parameters are filament diameter, nozzle diameter, nozzle temperature, bed temperature, printing speed, extrusion multiplier, layer height, and layer thickness.

The defects of green parts greatly influence the defects of the 3D object after debinding and sintering. However, to achieve the best densification, and consequently, better mechanical properties, the green 3D object may be submitted to cold isostatic pressuring (CIP).

2.2.5. Debinding

The debinding process mainly depends on debinding type. In the available publications, most debinding processes are composed of solvent debinding followed by thermal treatment, resulting in three main steps: solvent diffusion, dissolution of soluble binder, and finally diffusion from inside to outside of the remaining binder. An adequate debinding is based on a thermal cycle, where parameters such as heating rate, enough holding time, and suitable atmosphere must be selected [7], [10].

Currently, to reduce the environmental impact, the debinding consists in submitting the green to a thermal cycle.

Once the binder is eliminated, the so-called brown part is achieved which is characterized by the same volume and a reduction in mass with respect to the green part [5], [6], [11]. It is crucial to complete the binder and additives removal once residual carbon of organic degradation can affect the chemical composition of powder, surface morphology, and densification, and consequently cause significant defects during sintering [10].

After debinding, the powder particles should be close enough with the aim of potentiating the necking mechanism during sintering [7].

2.2.6. Sintering

Sintering is a thermal and pressure-activated transporting mechanism that contributes to a significant decrease of the free specific surface. The first step of sintering is the occurrence of necking between adjacent powder particles. Sintering at suitable temperatures and holding times contributes to a porosity decrease and a density improvement if the temperature does not promote phase transformations. However, it is important to remember that higher temperatures and longer holding times also increase grain size and, consequently, influence mechanical characteristics [7]. It is also important to control the cooling rate up to 500º to avoid phase transformation, reoxidation and nitrides/carbides formation that might negatively influence 3D object properties, like ductility and corrosion [5], [7].

Once consolidation occurs, and voids are closed, shrinkage of the sintered part is expected. This shrinkage depends on factors such as feedstock and green part homogeneity, and along X and Y direction has a similar behaviour of about 16% and along Z is close to 20%. It is important to consider shrinkage while drawing CAD of a 3D object to avoid achieving parts with dimensions lower than the required ones [12].

2.3. Stainless Steel (AISI) 316L

316L Stainless Steel is common steel due to its good corrosion and oxidation resistance, mechanical properties (Table 2.6), weldability, conformability, and non-magnetic behaviour. The L grade stands for low carbon steel (max. 0.03wt.% C). 316L primary constituents besides iron are chromium (16-18%), nickel (10-12%), and molybdenum (2-

3%), where chromium is responsible for steel oxidation/corrosion behaviour, and nickel's role is to promote austenitic phase at room temperature. 316L is suitable for medical applications due to its non-magnetic behaviour and biocompatibility. This steel is also widely beneficial in the military, chemical, and petrochemical industry, food processing, pharmaceutical equipment, wastewater treatment, etc.

Table 2.6. AISI 316L Mechanical Properties **[13]**.

AISI 316L	
UTS – Ultimate Tensile Strength	485 MPa
0,2% Yield Strength	170 MPa
Elongation	40%

2.4. Mechanical behaviour

The mechanical behaviour is greatly influenced by porosity. It is important to control porosity during MEX as one part is intrinsic to the process, but some porosity can also be avoided if its cause is known.

There is a study that considers that the inherent porosity can be a "relief valve" to release the product of binder degradation during the debinding stage [7]. According to (Wang et al., 2021)[14], pores initially form during the extrusion process of filaments and more pores arise while the binder system is removed during the debinding process. During printing, some pores intrinsic to the process are expected in the infill region and mostly between the infill and the layer boundaries [15].

After all the stages of SDS, some porosity will remain on the part, and its type and shape can suggest the cause that gave rise to it. In particular, if it has a spherical shape, then it was likely to happen during debinding thermal treatment. On the other hand, if it has a non-spherical shape, it was likely to get initiated during shaping due to the selected printing conditions [7].

2.4.1. Abrasive Wear – Ball-Cratering

Although formerly used to measure the thickness of thin coatings, the ball-cratering method can be used for the abrasion testing of surface-engineered materials.

This microabrasion test presents many advantages when compared with more conventional abrasion tests, including the ability to test small volumes of material and thin coatings. In addition, it is a simple, versatile, and easy to use method with low-cost equipment.

There are no specific standards for ball-cratering of metallic parts obtained by additive manufacturing processes. However, there is an approximated normative, ASTM G105-2020, that covers laboratory procedures for determining the resistance of metallic materials to scratching abrasion by means of the wet sand/rubber wheel test [22].

There is no bibliography where MEX specimens are subject to ball-cratering testing. Nevertheless, there are several studies where SLM and DED, i.e., additively manufactured, specimens are subject to dry wear testing [23]–[25].

The ball-cratering method consists of a ball rotating against a flat specimen with a slurry of fine abrasive particles passing at the contact interface [26]. The bibliography suggests that two types of abrasive wear modes are possible to be observed depending on factors, such as normal load, abrasive type, etc. Also, these modes can have a significant influence on the wear rate of a tribological system. Grooving abrasion is the result of particles that acted as fixed indenters by sliding over the surface of a specimen, so it is a two-body rolling wear mechanism. This mechanism is traduced by fine parallel grooves inside the crater. Rolling abrasion is observed when particles roll on the surface with no apparent directionality, so it is a three-body rolling wear mechanism [26], [27].

3. MATERIALS, METHODS AND TECHNIQUES

3.1. Raw Material

3.1.1. 316L Powder

Stainless steel (316L) powder used in this work was supplied by Osprey Sandvik®, belonging to batch 20D0872. According to the information provided by the supplier, 90% of the particles have a diameter <10 μm (D_{90} = 10 μm) and powder density is 7895.6 kg / m^3.

In MEX generally, powder consolidation does not occur through a liquid state sintering but by solid-state diffusion where a large free specific surface is welcome. Therefore, a powder with 10 μm D_{90} is within the range appropriate to promote efficient sintering. Figure 3.1 shows the powder particles size and powder particles size distribution observed in the scanning electron microscopy (SEM).

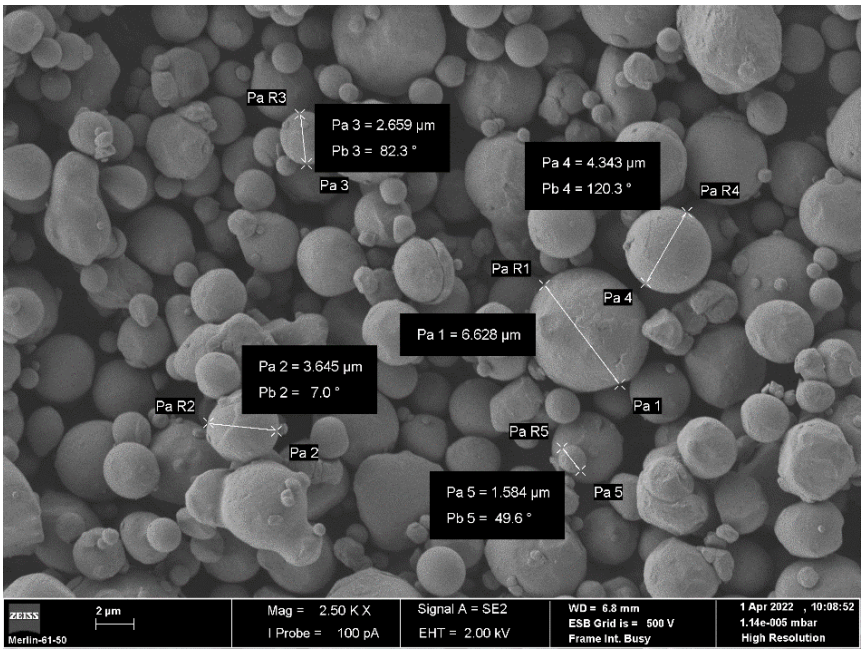

Figure 3.1. 316L powder particles and typical particle size (SEM).

According to Figure 3.2, powder particles showed generally a spherical shape leading to a shape factor close to 1.

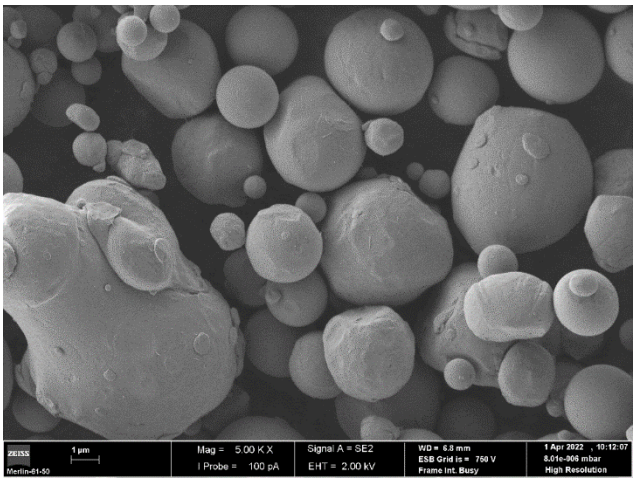

Figure 3.2. Detail of 316L powder particle characteristics (SEM).

X-ray diffraction (XRD) reveals a biphasic structure, mainly composed of austenitic phase, but with traces of martensite (Figure 3.3). The presence of a martensitic phase could be explained by the atomization process and its pressure variation.

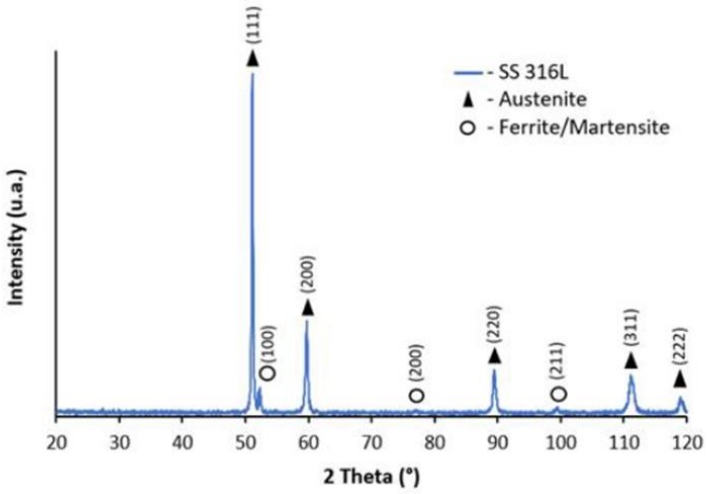

Figure 3.3. X-ray diffractogram of 316L powder.

3.1.2. Binder and Additives

The polymeric part of the feedstock was composed of a master binder M1, a thermoplastic elastomer (TPE), and a plasticizer (Table 3.1).

Table 3.1. Binder and Additives Densities.

Densities	
M1	$970\ kg\ /\ m^3$
TPE	$910\ kg\ /\ m^3$
Plasticizer	$965\ kg\ /\ m^3$

M1 was a master binder with exceptional behaviour in powder injection moulding (PIM), with similar goals to the filament of MEX, and owing to its suitableness to work with thermal debinding [9], [28]. It is composed mainly of polyolefin and polyoxymethylene copolymer (POM). TPE was the backbone polymer with the function of holding the green part shape until the sintering stage. The plasticizer has the aim to enhance filament flexibility.

With this organic system, it was possible to obtain a suitable relationship between green body integrity, flowability, and filament flexibility.

3.2. Methodology

3.2.1. Feedstock Preparation

The feedstock was prepared in a Brabender® Plastograph® W50 mixer that has a 3.8×10^{-5} m^3 volume chamber. In this work, the mixtures were composed of 60 vol%. of metallic powder and 40 vol%. distributed between M1, TPE and plasticizer. Mixtures with this 316L metallic volume composition were optimized in a previous study [3]. Since the powder density and the volume percentage of the different components were known, the mass of each component to be introduced in the chamber was calculated using equation (3.1):

$$\text{mass}_{\text{Component}}[\text{kg}] = 3.8 \times 10^{-5}\ \text{m3} \times \text{vol.}\,\%_{\text{Component}} \times \rho_{\text{Component}} \quad (3.1)$$

Steel, M1, and additives were weighted on an Ohaus® AP250D balance in proper containers (Figure 3.4) and then introduced into the mixing chamber as follows: M1, TPE, plasticizer, 316L. Mixing was carried out at 190ºC temperature, using a 30-rpm blade rotation speed.

Figure 3.4. Organic materials before introduction into the mixer to power blending (feedstock).

The feedstock was then granulated in a Hellweg® Mill and introduced in the feeding hopper of the extrusion equipment (filament production).

3.2.2. Extrusion

The Brabender® GmbH & Co. extruder is composed of 5 heating zones and a single screw mechanism that receives and forces the feedstock to pass through a 1.75 mm nozzle. This process occurs with ascending temperature in the 5 heating zones (160ºC, 165ºC, 175ºC, 180ºC, and 180ºC), and with a screw rotation speed of around $3 - 4$ rpm. Approximately 1.70 kg of filament was produced.

3.2.3. 3D Printing

The software used to obtain the specimens' 3D models was Autodesk® Inventor® Professional 2022. Subsequently, the STL file was exported to PrusaSlicer 2.4.0 where the G-Code was generated. First of all, some printing parameters were tested, and afterwards, G-Code was loaded in Repetier-Host, and specimens were printed with Prusa MK3S using the following parameters (Table 3.2):

Table 3.2. Some of the Printing parameters.

Fixed Parameters		
Nozzle Temperature	Bed Temperature	Printing Speed
190ºC	60ºC	30 mm/s
Nozzle Diameter	Layer Height	Fill Pattern
0.4 mm	0.2 mm	Rectilinear
Variable Parameters		
Extrusion Multiplier		Diameter
1.00 - 1.10 According to Diameter Variations		1.75 mm

3.2.4. Debinding & Sintering

Debinding and sintering were performed using an electrical oven (Termolab) with a binder removal system. An argon atmosphere, during different holding times was tested, with the aim of evaluating the influence on the densification process. The thermal cycles were defined based on previous studies where 316L powder was the metallic material.

3.3. Characterization techniques

3.3.1. Density meter (Archimedes' Method)

Primary, 10 random filament sections with lengths between 2 and 4 cm were chosen and weighted in an Ohaus® AP250D balance. Once the filament sections were going to be submerged in water, it was necessary to coat them with varnish (V33 verniz exterior Marinho Incoloro - 0,75L - 009778) with a density of 900 $kg\ /\ m^3$, so water would not fill the pores resulting in incorrect values. After coating, it was necessary to wait 24 hours which was the time needed for the varnish to dry. Each section was submitted to two weight measurements again, one after coating and the other while submerged in water.

3.3.2. Optical Microscopy

The OM microscope uses visible light and a system of lenses to magnify images of small samples.

In the present study, the equipment Leica DM4000 M LED with a maximum magnification of 1000x, was used to observe the surface of the sintered 3D objects and, forwardly, the surface of the 3D objects and WM 316L specimen after ball-cratering microabrasion tests. This equipment has a LEICA MC190 HD camera connected.

3.3.3. Scanning Electron Microscopy

SEM consists in projecting and scanning a focused stream of electrons over a surface to produce an image. The electrons interact with the surface, producing different signals (secondary electrons, backscattered electrons, and X-rays) that can be used to obtain information about its topography and chemical composition.

Two SEM microscopes were used. The first one (from IPN[1]) is a ZEISS Merlin/ Gemini 2 microscope equipped with EDS with a beam energy of 10 kV, and it was used to observe raw powder, filaments' cross-sections, and filaments surface with different magnifications. The MEX 3D objects and WM material after the micro-abrasion tests were also analysed using this microscope. The second one, available at DEM[2] UC, and also equipped with EDS with a beam energy of 15 kV, was used to observe sintered parts' surface topography and chemical composition.

3.3.4. Microtomography

The equipment Bruker SkyScan 1275 X-Ray with the respective dedicated software was used to perform microtomography. An acceleration voltage of 100 kV and a beam current of 100 μA (which are associated with maximum equipment power) were set while using a 1 mm Copper filter. The pixel size was 12 μm and 601 images were acquired at a 0,4º angular step with 5 frames per step using an exposure time of 245 ms.

[1] Instituto Pedro Nunes
[2] Department of Mechanical Engineering

Microtomography was performed on the filament, green parts, and sintered ones to observe porosity and defects distribution and evolution along the MEX process.

3.3.5. Ultramicrodurometer

Hardness testing consists in evaluating the material resistance to localized plastic deformation. In this work, hardness and Young's modulus were evaluated by depth-sensing indentation using Fischerscope equipment (H100). Each specimen was subject to 24 loading/unloading measurements using a maximum load of 1000 mN (corresponding to ~100 g) applied by a Vickers indenter. During the test, the load was increased in steps until the nominal test load was reached and maintained during 30 s. During loading/unloading the number of steps was 60 and the time between each step was 1 second. At the end of the test, the 0.4 mN minimum load was maintained during 30 s in order to allow thermal drift correction. The data were treated using software developed at DEM UC.

3.3.6. Ball-Cratering

The preliminary tests were performed according to Vilhena et al. [26] conditions. MEX 3D objects and WM were subjected to 100, 200, 300, 400, and 500 rotations of the ball which corresponds to a sliding distance of 8, 16, 24, 32, and 40 m, respectively. The linear velocity of the ball rotating against the specimen was 0.1 m/s, corresponding to approximately 75 rpm (once the ball diameter is 25.4 mm). A 0.2 N normal load was applied using dead weights in the hanger arm.

Silicon carbide (SiC) abrasive particles (see Appendix A) were used to produce an abrasive slurry with a concentration of approximately 20 vol.%. This slurry was continuously stirred using a magnet and fed at the interface specimen/ball drop by drop.

The laboratory where the tests occurred was kept at a room temperature of 29 ± 2°C and 49 ± 10% relative humidity.

The available equipment at the DEM/FCTUC is the same used in a previous study [26]. A brief schematic of the apparatus and its elements are described in Figure 3.5 and Table 3.3.

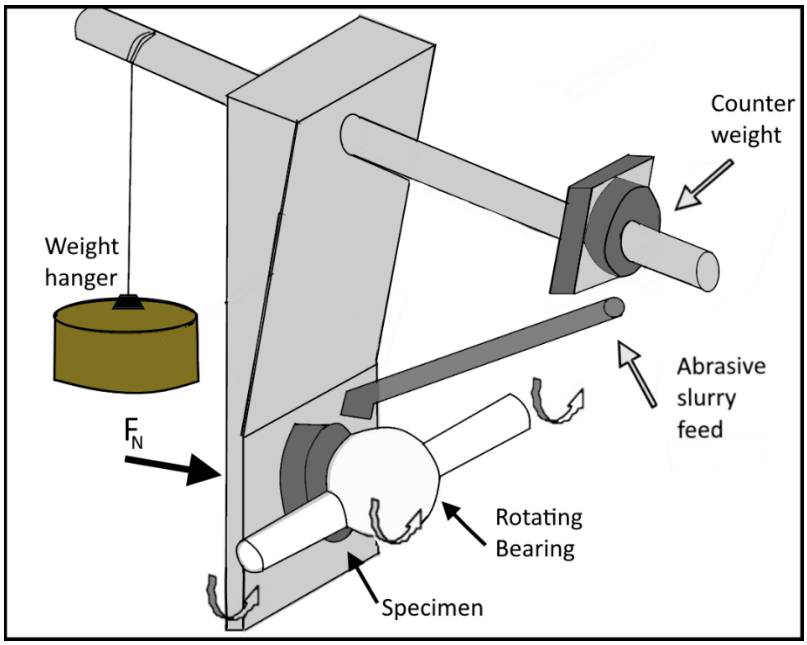

Figure 3.5. Schema of the ball-cratering equipment **[26]**.

Table 3.3. Ball-cratering equipment parts.

Elements of the testing equipment	
AISI 52100 Bearing	Steel ball with 25.4 mm diameter. Wears the specimen while rotating.
Shaft	Connects the motor to the ball.
Motor (variable speed)	Produce shaft rotation.
SiC based slurry	Increase the abrasive wear on the specimen. Is continuously fed drop by drop.
Weight hanger	May hold dead weights allowing the application of a normal load in the interface specimen ball.

After the ball-cratering tests, the worn surfaces were observed by optical microscopy and SEM, while profilometry analyses were carried out to measure the wear volume. The measurements were performed using a Mitutoyo Surftest Sj-500 apparatus and the wear volume was determined as described by Vilhena et al. [26], using equation (3.2) where b and R correspond to the average chord length of the spherical cap and the ball radius, respectively:

$$V = \frac{\pi b^4}{64R}, b << \mathrm{R} \quad (3.2)$$

4. RESULTS AND DISCUSSION

4.1. From powder to feedstock

4.1.1. Feedstock production

316L stainless steel, binder and additives were introduced into the mixing chamber, and torque was recorded for five mixtures with 60%vol. of metallic powder (chapter 2). According to Figure 4.1, the steady regime, when the homogeneous distribution among metal powder, binder and additives was achieved, is attained at the 30th minute of mixture, corresponding to a torque of 4.26 N.m.

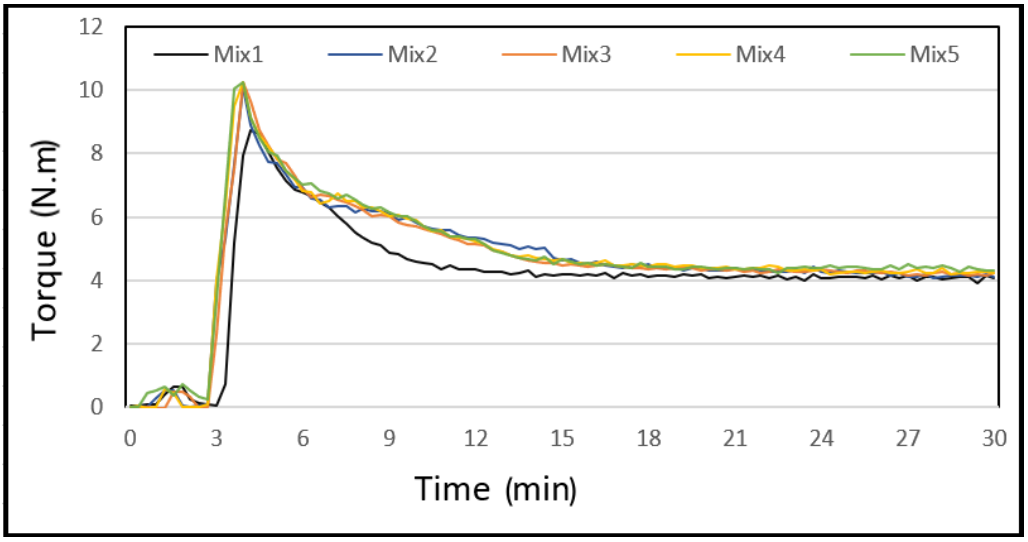

Figure 4.1. Torque as function of mixing time (5 mixtures with same content of constituents).

Maximum torque was reached during the introduction of metal powder because each particle was not “coated” by the binder yet, so there was significant interparticle friction. There was a small peak at the beginning that matches with the addition of TPE.

Overall torque has a slight increase from 1st to 5th mixture. Once all 5 mixtures had the same composition, the mixing chamber was only cleaned before the 1st mixture and after the 5th one meant that the small torque increasing from 1st to 5th mixture could be explained by the remaining residues that by lasting in the chamber would slightly affect the calibration and subsequent torque measurements.

Figure 4.2 shows the appearance of the mixture after being removed from the mixing chamber (left side) and after granulation (right side).

Figure 4.2. Feedstock A) after mixing, and B) after granulation.

4.2. From feedstock to filament

4.2.1. Filament Production

The filament was successfully extruded from the feedstock and, as required, it was easily coiled (Figure 4.3). To maintain a constant diameter during the extrusion, the height between the extruder nozzle and the plate where it was collected has remained constant. Ten random samples of filament were selected and their diameter measured using a calliper, resulting in a diameter of $1.72 \pm 0.07mm$.

Figure 4.3. Filament.

4.2.2. Green Filament Characterization

4.2.2.1. Density (Archimedes' Method).

The density of the green filament was measured with and without water impermeable varnish. The test conditions and abbreviations used are summarized in Table 4.1.

Table 4.1. Starting conditions and abbreviations.

		Designation	
T_{room} [°C]	21	ρ - Density	
$\rho_{water\ at\ 21°C}$ [kg/m^3]	998	**m** - Mass	**V** - Volume
$\rho_{varnish}$ [kg/m^3]	900	**W** - With	**Ww** - Without
$\rho_{theoretical}$ [kg/m^3]	(eq. 4.2.) 5121	**v** - Varnish	**S** - Submerged

Using the previously measured masses, m_v could be obtained by subtracting m_{Wwv} from m_{Wv}. Then, resorting to Archimedes' Method (4.1):

$$\rho_{Wv} = \frac{m_{Wv}}{m_{Wv} - m_{SWv}} \times \rho_{water\ at\ 21\,°C} \tag{4.1}$$

From (4.1), ρ_{Wv} was known and it was possible to obtain V_{Wv} by the quotient of m_{Wv} by ρ_{Wv}. Once the varnish density is known (Table 4.1), by dividing m_v by ρ_v it was possible to find V_v, and subsequently, by subtracting it to V_{Wv} the V_{Wwv} value was acessed. Finally, it was possible to obtain a value for each filament density (ρ_{Wwv}) dividing m_{Wwv} by V_{Wwv}.

To calculate relative density, ($\rho_{theoretical}$) must be calculated by (4.2); and the relative density results from the ratio $\rho_{Wwv} / \rho_{theoretical}$.

$$\begin{aligned}\rho_{theoretical} &= 0.6 \times \rho_{316L} + 0.3 \times \rho_{M_1} + 0.07 \times \rho_{TPE} + 0.03 \times \rho_{Plasticizer} \\ &= 5121\ kg/m^3\end{aligned} \tag{4.2}$$

Table 4.2. Relative densities by Archimedes' Method.

Piece Number	m_{Wwv} [g]	m_{Wv} [g]	m_v [g]	m_{Swv} [g]	ρ_{Wv} [g/cm^3]	V_{Wv} [cm^3]	V_v [cm^3]	V_{Wwv} [cm^3]	ρ_{Wwv} [g/cm^3]	Relative Density
1	0.3227	0.3262	0.0035	0.2580	4.7734	0.0683	0.0039	0.0644	5.0072	97.78%
2	0.4127	0.4163	0.0036	0.3323	4.9460	0.0842	0.0040	0.0802	5.1479	100%
3	0.3766	0.3804	0.0038	0.3028	4.8923	0.0778	0.0042	0.0735	5.1215	100%
4	0.3034	0.3063	0.0029	0.2419	4.7467	0.0645	0.0032	0.0613	4.9489	96.64%
5	0.2574	0.2603	0.0029	0.2079	4.9576	0.0525	0.0032	0.0493	5.2229	100%
6	0.3170	0.3210	0.0040	0.2556	4.8984	0.0655	0.0044	0.0611	5.1894	100%
7	0.3572	0.3600	0.0028	0.2877	4.9693	0.0724	0.0031	0.0693	5.1519	100%
8	0.2673	0.2694	0.0021	0.2146	4.9062	0.0549	0.0023	0.0526	5.0840	99.28%
9	0.3155	0.3191	0.0036	0.2527	4.7961	0.0665	0.0040	0.0625	5.0453	98.52%
10	0.2837	0.2852	0.0015	0.2288	5.0466	0.0565	0.0017	0.0548	5.1726	100%

Overall, relative density was almost similar in the 10 segments of filament (samples) which could validate the tendency to homogeneity of the filament. In addition, the relative density was approximated to 100% meaning a low porosity. Other studies with the MEX process using stainless steel (316L, 17-4PH) and Ti-6Al-4V report similar filament's relative densities [29]–[31].

4.2.2.2. Homogeneity (microtomography)

μCT and SEM allow filament homogeneity and internal porosity levels before proceeding with 3D printing (MEX) to be evaluated. Figure 4.4 shows a filament cross-section (40x), and Figure 4.5 shows two regions in the cross-section: (A) closer to the centre and B) in the periphery (500x and 250x), respectively. The SEM images exhibit a suitable distribution of binder around the powder, meaning that all metallic particles are surrounded with binder, and suggest low powder agglomerations. It is possible to observe that the powder particles are close to each other, which is favourable for solid diffusion during sintering.

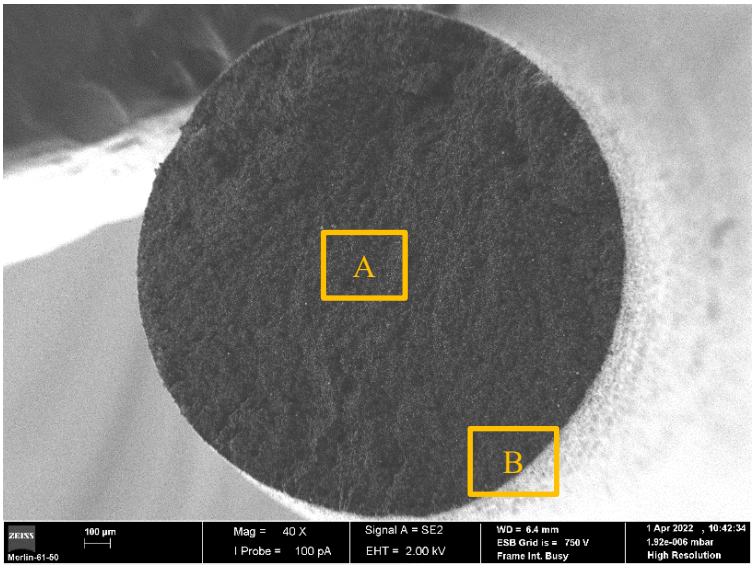

Figure 4.4. Cross-section of the filament (SEM), 40x.

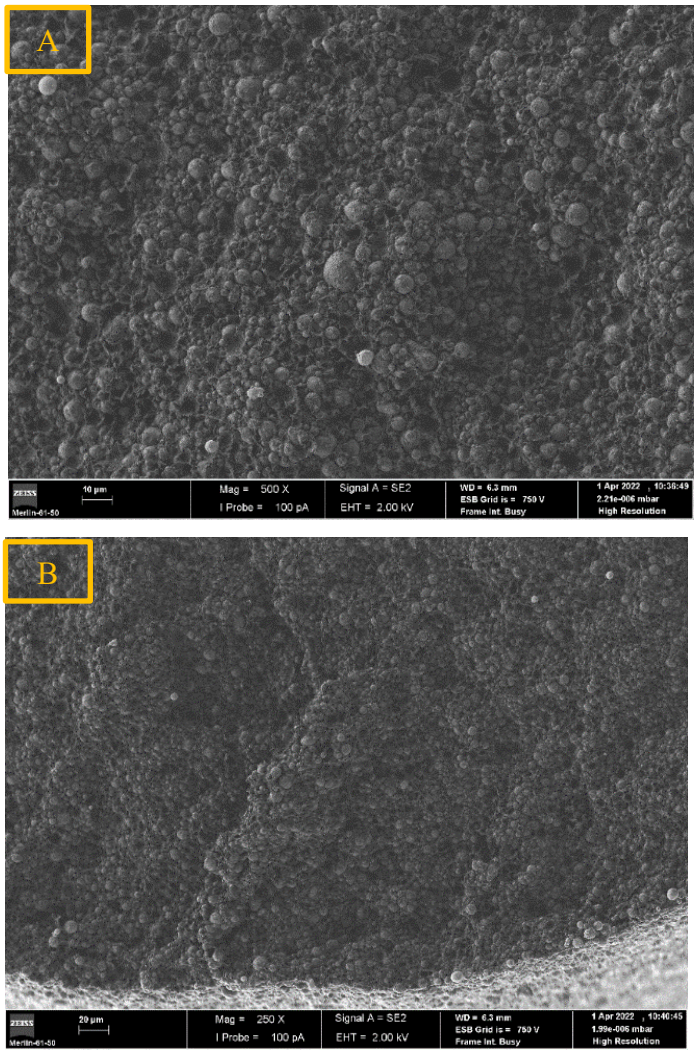

Figure 4.5. Central region of the filament (A), 500x, and periphery of the filament,250x (SEM).

One of the main advantages of μCT is the possibility of getting access to the inside filament without damaging it. Also, μCT provides a resolution of 10 μm. Figure 4.6 and Figure 4.7 highlight 3-plane and volumetric views of the filament.

By observing both figures it is possible to notice a consistent diameter and a low porosity, in accordance with the relative densities of the filament obtained with Archimedes' method. Figure 4.6 and Figure 4.7 also reveal a few pores with an elongated geometry in the extrusion direction, suggesting that pores might have surged during the extrusion process.

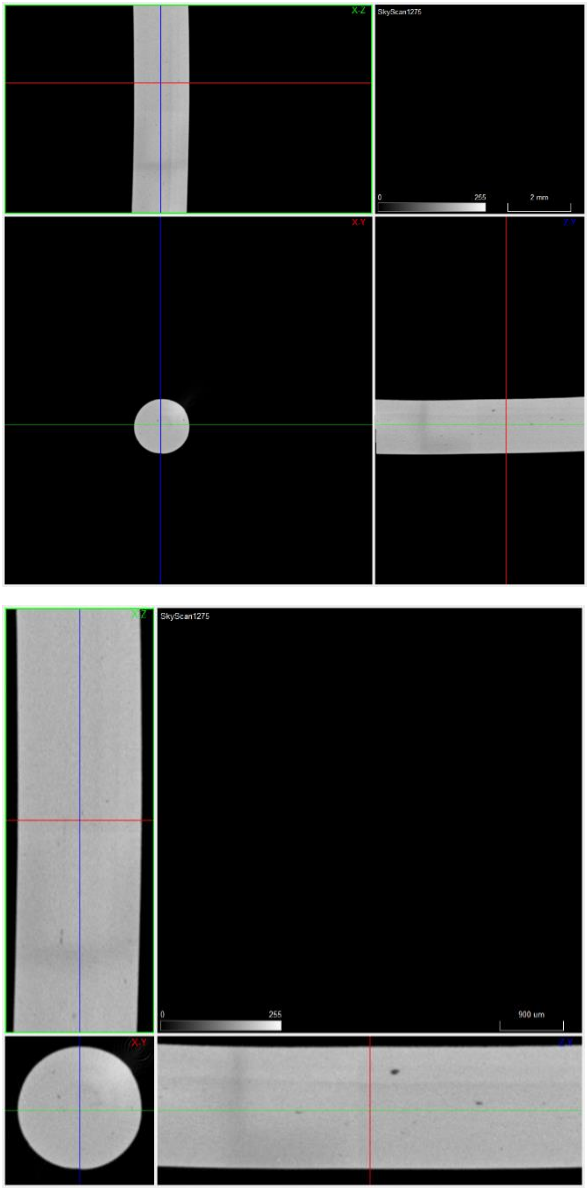

Figure 4.6. μCT 3-plane views of filament.

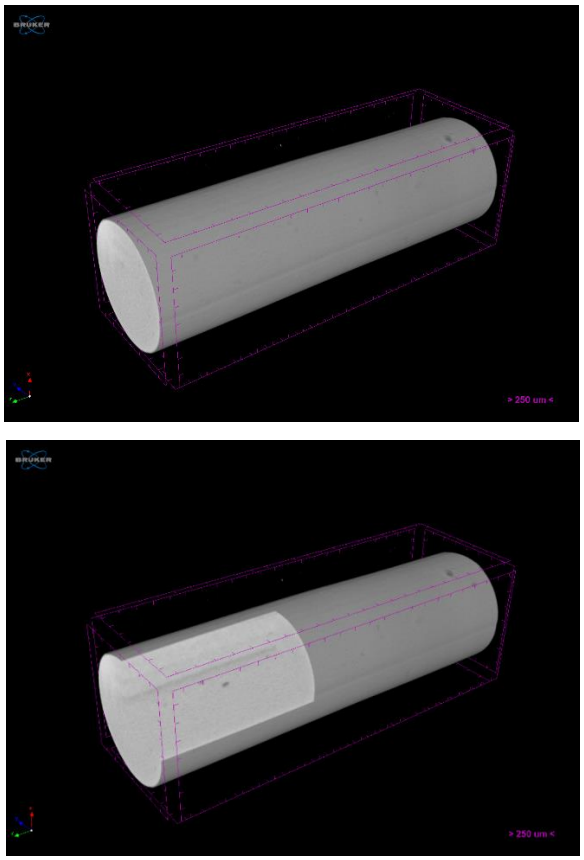

Figure 4.7. μCT 3D-view of the filament.

4.3. Shaping 3D object

4.3.1. Computer-Aided Design (CAD) and Standard Tessellation Language (STL)

The CAD file is the digital representation of the desired 3D object (Figure 4.8) and the STL is a file format used for describing the surface of an object as a triangular mesh.

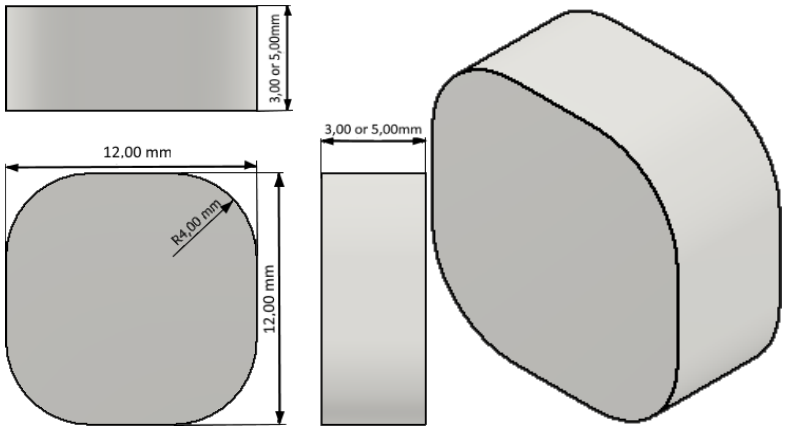

Figure 4.8. Dimensions of an object with simple geometry in CAD file.

During sintering, there is shrinkage of the brown (after debinding), so it was necessary to oversize it before G-Code generation to compensate for future shrinkage and attain the desired dimensions of the final 3D object. This oversizing can be done either in a CAD or an STL file; in the present study, it was adjusted in the STL file (Figure 4.9). In order to estimate the shrinkage percentage, a few test printed parts were submitted to debinding and sintering stages. Along the x and y-axis shrinkage was very similar to 14%, while along the z-axis the value was approximately 20%. Bibliography also reports the different behaviour along the z-axis relative to the x and y-axis, and similar shrinkage results that depend on specimen size and especially on metal volumetric percentage [4], [32]–[36].

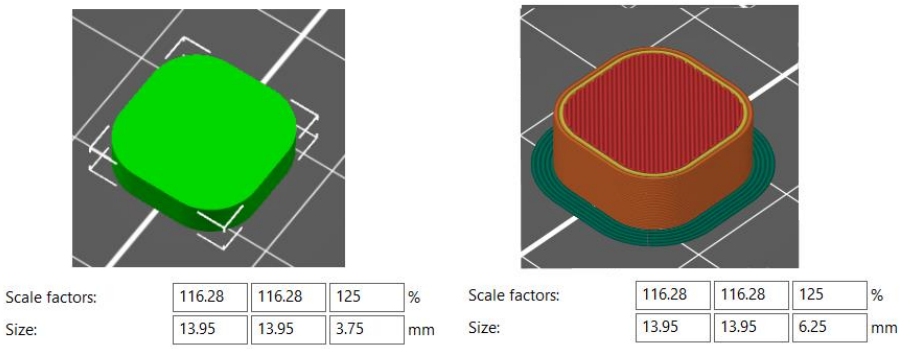

Figure 4.9. Dimensional shrinkage adjustment for 3 mm (left) and 5 mm (right) thickness of 3D object in the STL.

4.3.2. 3D Printing

Good quality of green parts depend on the careful selection of the 3D printing parameters. Table 4.3 summarizes the parameters that led to high-density 3D objects. Since the 3D objects were printed with similar volume, those that presented higher mass were the ones that would most likely have the greatest density.

Table 4.3. 3D print parameters selected in PrusaSlicer 2.4.0.

Layer Height	No. of Perimeters	Fill Pattern (100% Infill)
0.2 mm	2	Rectilinear
Brim	Printing Speed	Nozzle Diameter
Outside Brim 2mm Width	30 mm/s	0.4 mm
Nozzle Temperature	Bed Temperature	Multiplier
190ºC	60ºC	1st layer – 1.00 Other layers 0.98 to 1.06

After generating the G-code, which is the most widely used computer numerical control (CNC) programming language, it was loaded in Repetier-Host which was used to control in real-time printing parameters such as extrusion multiplier. Despite being consistent, filament diameter suffered some slight variation, so it was necessary to keep measuring it with a calliper to properly adequate extrusion multiplier, leading to the highest possible density 3D object. When the filament diameter was between 1.75 and 1.80 mm,

other layers (Table 4.3) were left with a 1.00x multiplier unless there was material getting accumulated in the nozzle in which case it was necessary to lower the multiplier to 0.98x. Nonetheless, when the diameter was in the range of 1.68-1.75 mm, an inverse multiplier-diameter relationship was used for other layers. A 190ºC nozzle temperature with proper tightening of the feeding mechanism bolt was enough to guarantee a continuous extrusion. A 60ºC bed temperature and 2 mm width outside brim were suitable to promote adhesion and avoid warpage.

4.3.2.1. Green 3D Object

Specimens with different geometries (Figure 4.10), were 3D printed. The observations in naked eye reveal surfaces of the as-printed specimens in general with no space visible, either in infill lines or between infill and perimeters. A small overlap of material is observed in the infill lines since the multiplier was optimized to obtain the highest possible green density. A better perspective of the green parts was highlighted by microtomography. Table 4.4 and Table 4.5 summarize the dimensions and weight of the selected specimens for specimens with 3 and 5 mm. These values were selected to guarantee an efficient debinding.

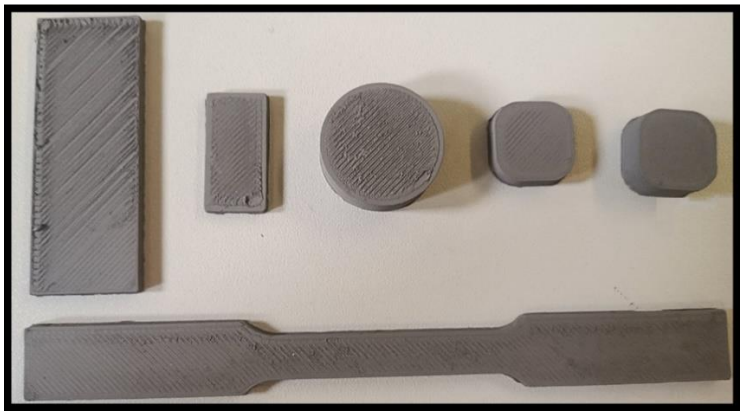

Figure 4.10. Examples of printed green specimens.

Table 4.4. Dimensions and weight of the printed green specimens (thickness ≈ 3 mm).

3 mm				
Specimen	X (mm)	Y (mm)	Z (mm)	Weight (g)
1	14.23	14.20	3.78	3.260
2	14.28	14.02	3.74	3.034
3	14.13	13.97	3.76	3.103
4	14.31	14.18	3.75	3.191
5	14.22	14.19	3.84	3.292
6	14.30	14.29	3.80	3.320

Table 4.5. Dimensions and weight of the printed green specimens (thickness ≈ 5 mm).

5 mm				
Specimen	X (mm)	Y (mm)	Z (mm)	Weight (g)
7	14.31	14.09	6.08	5.376
8	14.17	14.15	6.13	5.373
9	14.26	14.24	6.07	5.104
10	14.35	14.29	6.07	5.161
11	14.29	14.26	6.21	5.491
12	14.22	14.15	6.07	5.371

Figure 4.11 and Figure 4.12 show microtomographies of several 3 and 5 mm thickness green specimens. The 1, 5, 6, 7, 8, 11, and 12 had the lowest porosity. In specimens 2, 3, 4, 9, and 10 porosity was more visible. Nevertheless, the homogeneity of the specimens is perceptible.

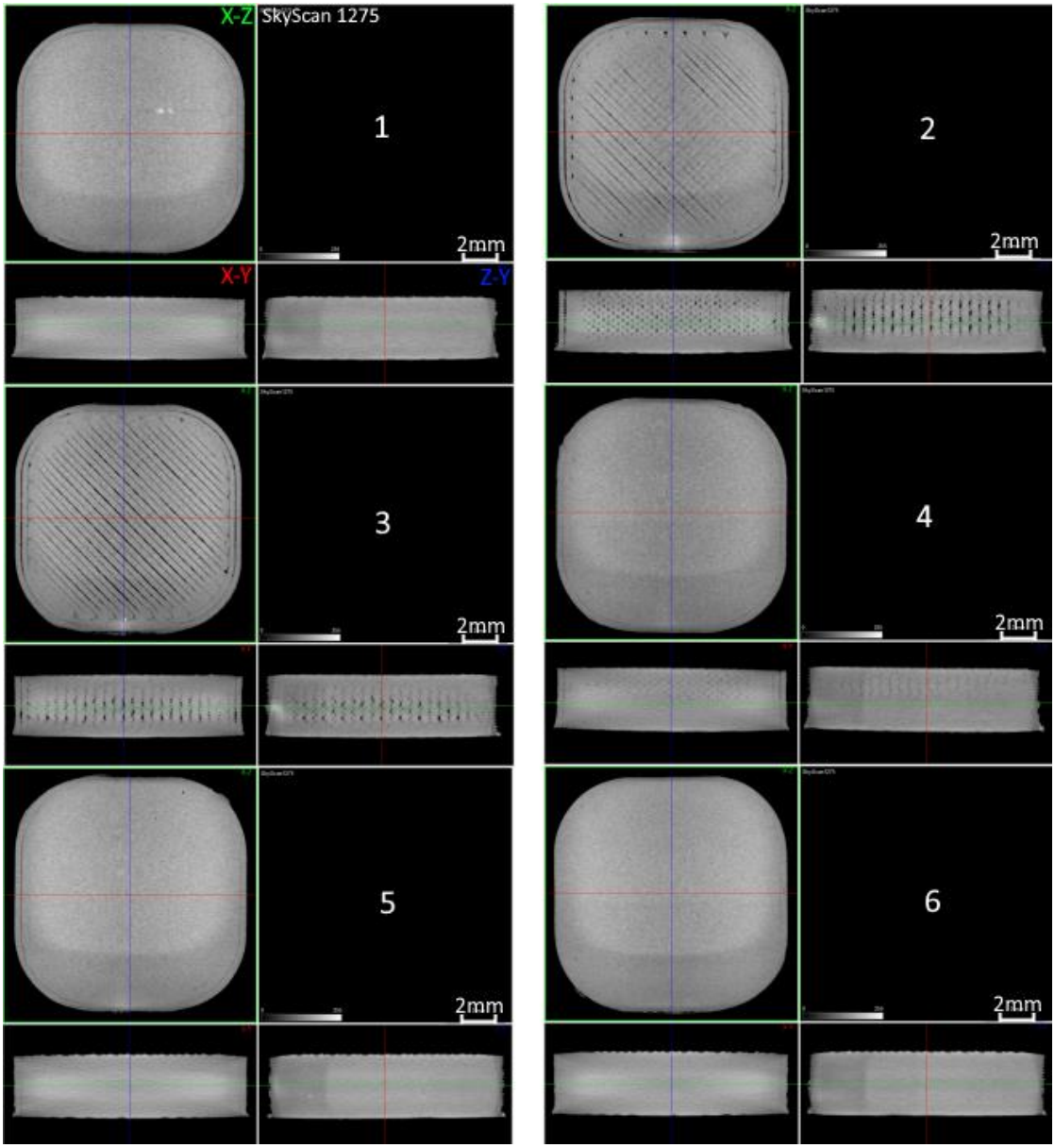

Figure 4.11. μCT images of green specimens with 3 mm thickness.

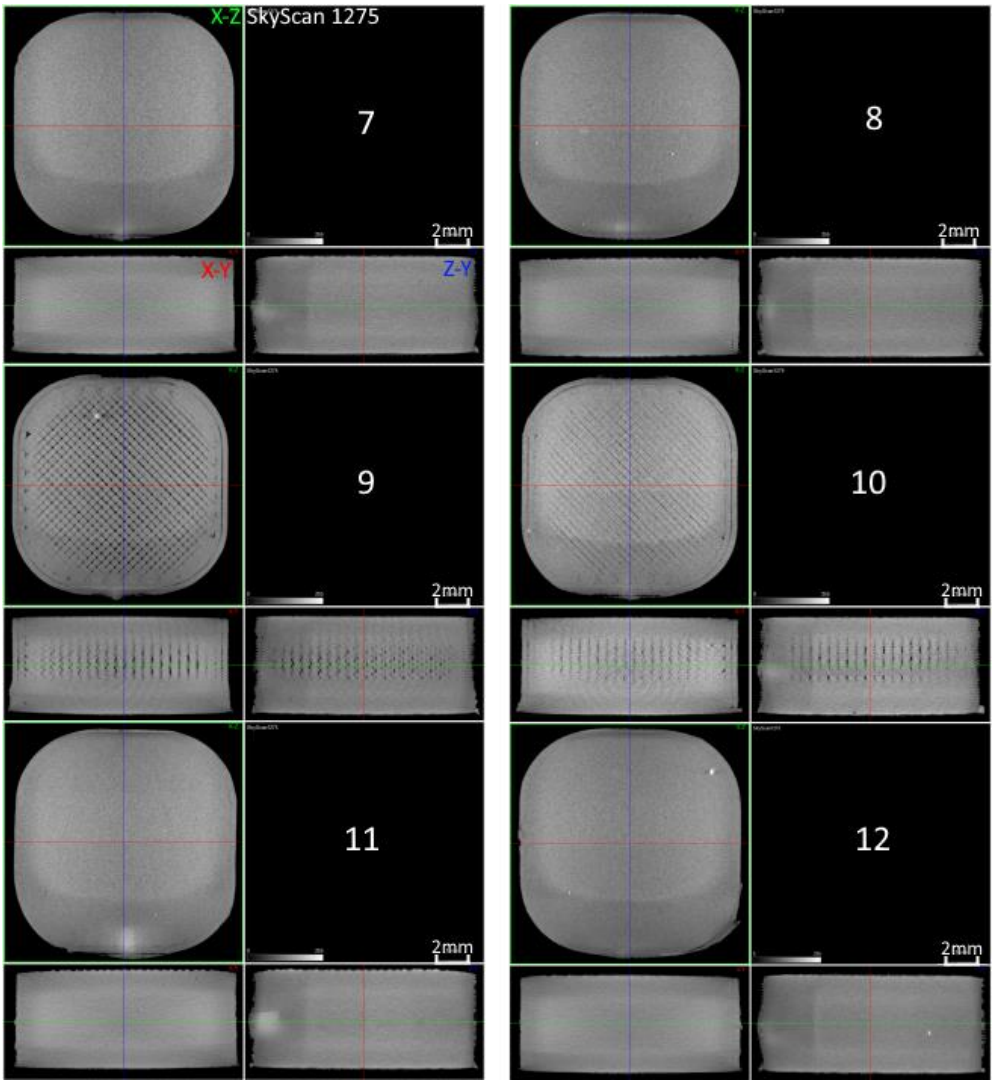

Figure 4.12. μCT images of green specimens with 5 mm thickness.

Looking at the X-Z plane it is possible to detect pores (> 10 μm), that follow the perimeter contour, between the first and second lines of the perimeter. In other specimens (2, 3, 9, and 10), they are also observed between the second perimeter line and the infill. Pores between the second perimeter and infill are almost unnoticed in specimens 1, 4, and 5, and got imperceptible in specimens 6, 7, 8, 11, and 12. Looking along the thickness of the specimen (X-Y and Z-Y planes) it is also notable the same type of porosity between the first and second perimeter layers for all the specimens with the exception of the 11 and 12 specimens, where it is almost imperceptible. Porosity between the second perimeter layer and infill for specimens 2, 3, 4, 9, and 10 is detected, and it is almost imperceptible in specimen 1, while for the other specimens it seems absent. The above-mentioned types of porosity are inherent to the process. Not only do printing lines have ellipse cross-sections,

but also when the printer is reversing the direction the U-turn is not sharp enough as printers compensate for all sharp corners with curves as reported by Y. Tao et al. [37]. Figure 4.13 (bottom) depicts porosity created by two concentric perimeter lines and layers and compares it with specimen 2, μCT (X-Y plane). Figure 4.13 (top) depicts porosity in the region where infill contacts with the perimeter.

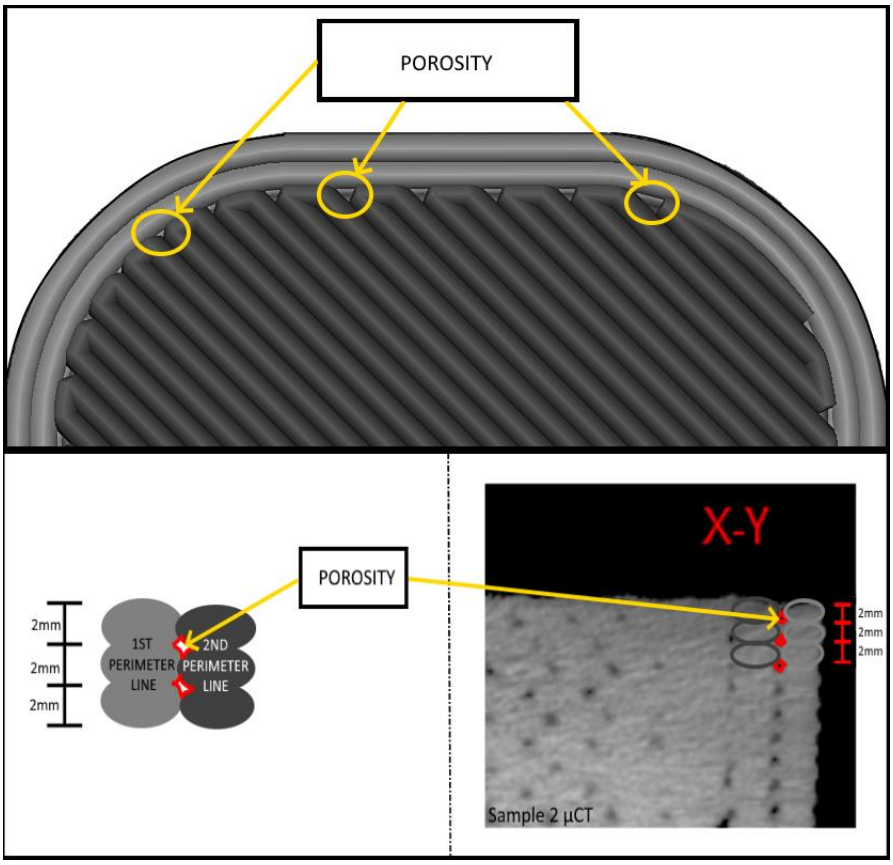

Figure 4.13. Porosity between consecutive perimeter lines and layers (bottom), and between perimeter line and infill (top).

The specimens 2, 3, 4, 9, and 10 voids between printing lines (infill) are very pronounced, and probably the cause is unsuitable compensation of extrusion multiplier which should have been higher than the selected one (within the range specified in printing parameters). It is also evident for every specimen that the first layers are always very dense. This results from an inherent shaping characteristic which is the first layer squeezing. In specimens 1, 3, 8, 9, 10, 11, and 12 there are white points (in the X-Z plane) as well as in specimens 5 and 12 (in the Z-Y plane). These artifacts were probably due to foreign particles that remained in the extruder channels even after the cleaning procedure.

4.4. Debinding and Sintering

Debinding and sintering of the greens 1, 2, 7, and 8 were performed under an argon atmosphere, and the debinding thermal cycle was typical for the binder and additives used in the present study (Figure 4.14). The debinding heating rate was 1 °C/min, with different steps and a total duration of 17 hours up to 600ºC. Holding times of 120 min at 250ºC, 90 min at 300 and 420ºC, and 60 min at 450 and 600ºC were selected to guarantee proper organic constituents' elimination. In what concerns sintering, the heating rate was 2ºC/min, with a duration of 7 hours and 55 minutes consisting of heating up to 1250ºC. Holding times of 30 min at 750ºC, 900ºC, and 1100ºC, and of 60 min at 1250ºC. A controlled cooling rate of up to 500ºC was performed.

Specimens 1 and 2 (thickness = 3 mm) presented a porous surface, while specimens 7 and 8 (5 mm height) cracked during the debinding and sintering steps. This is due to problems in the elimination of the gas resultant from the ustulation of organic constituents during the debinding (Figure 4.15). In fact, one of the limitations of the MEX, like in powder injection moulding (PIM), relies on the size of the 3D objects, because defects such as cracks and large deformations will appear as size increases [38].

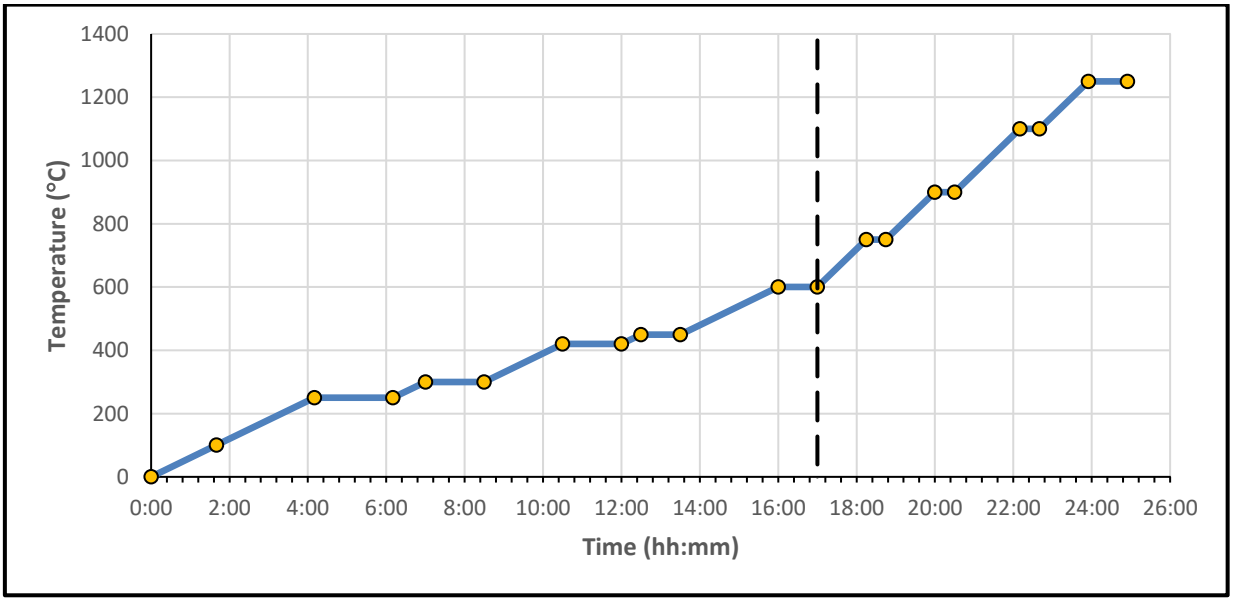

Figure 4.14. Debinding and sintering thermal cycle used in specimens 1, 2, 7, and 8.

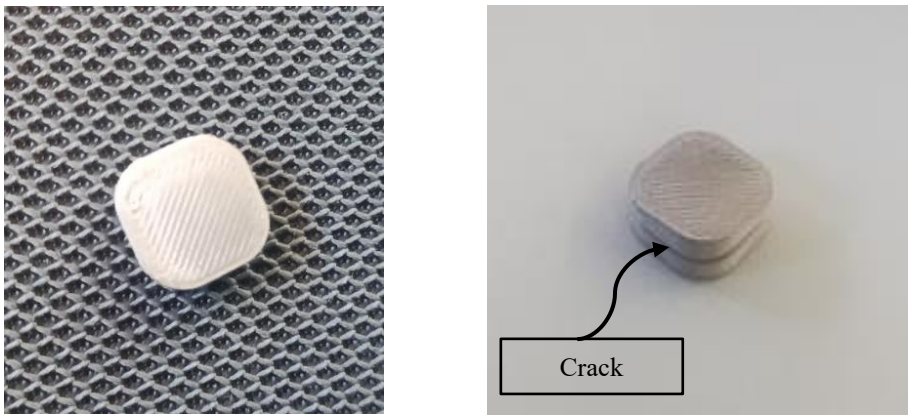

Figure 4.15. 3mm (left) and 5mm specimens (right) aspect after debinding and sintering

4.5. Post-Sintering 3D objects Characteristics

After sintering 3D objects of specimens 1 and 2 (3 mm thickness) were polished (Figure 4.16) and observed (Figure 4.17). Porosity is detected in both polished surfaces, and voids between lines were observed only in the 3D object of specimen 2.

Figure 4.16. Polished 3D objects (1 and 2).

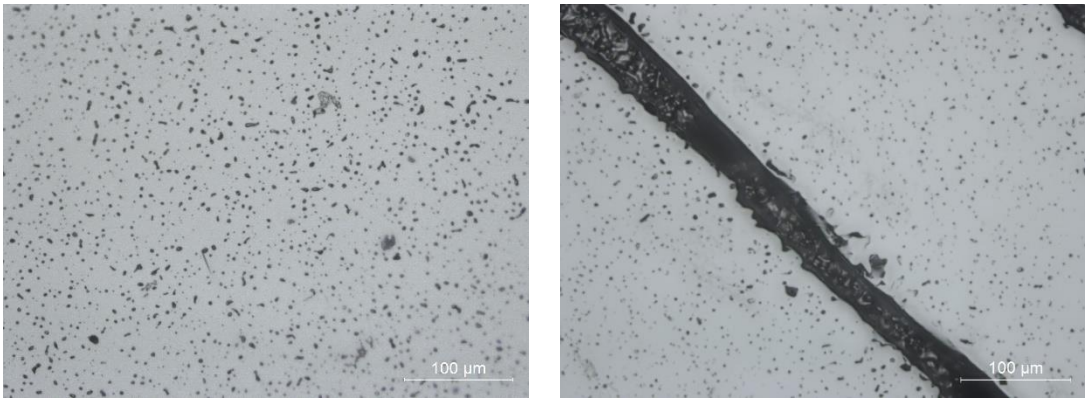

Figure 4.17. 3D object of specimens 1 (left) and 2 (right) highlighting porosity (OM).

Table 4.6 contain data, such as the sintered dimensions of the 3D objects, weight, weight loss versus green, and shrinkage along XYZ.

The 3 mm (thickness) shrinkage of the 3D objects was close to the expected 14%. Moreover, along the Z axis, there is some unconformity. The even lower value of shrinkage along z for 3D object 1 resulted from its inner crack (Figure 4.20).

Table 4.6. Dimensions and weight of 3 mm (thickness) 3D objects.

3 mm						**Shrinkage [%]**		
3D Object	X [mm]	Y [mm]	Z[mm]	weight[g]		X	Y	Z
1	12.48	12.48	3.32	3.029	-7.11%	12.30%	12.11%	12.17%
2	12.43	12.28	3.19	2.818	-7.11%	12.34%	12.41%	14.71%

Figure 4.18 and Figure 4.19 show a plane μCT of 3D objects 1 and 2, respectively. In 3D object 1, it is possible by μCT to observe cracks inside. Different factors like the organic constituents had no possibility to get away during debinding; insufficient argon flow or low holding time during the debinding and sintering cycle. In 3D object 2, by μCT it is possible to observe higher porosity levels than in 1, which may contribute to increasing the efficacity of the debinding step. However, the observed porosity follows the printing lines at the centre, and the perimeters at the periphery, meaning that their cause is not during the debinding and sintering cycle. Additionally, these images (especially 3D object 2) are a demonstration that the debinding and sintering cycles do not contribute to eliminating defects resulting from printing, as in PIM.

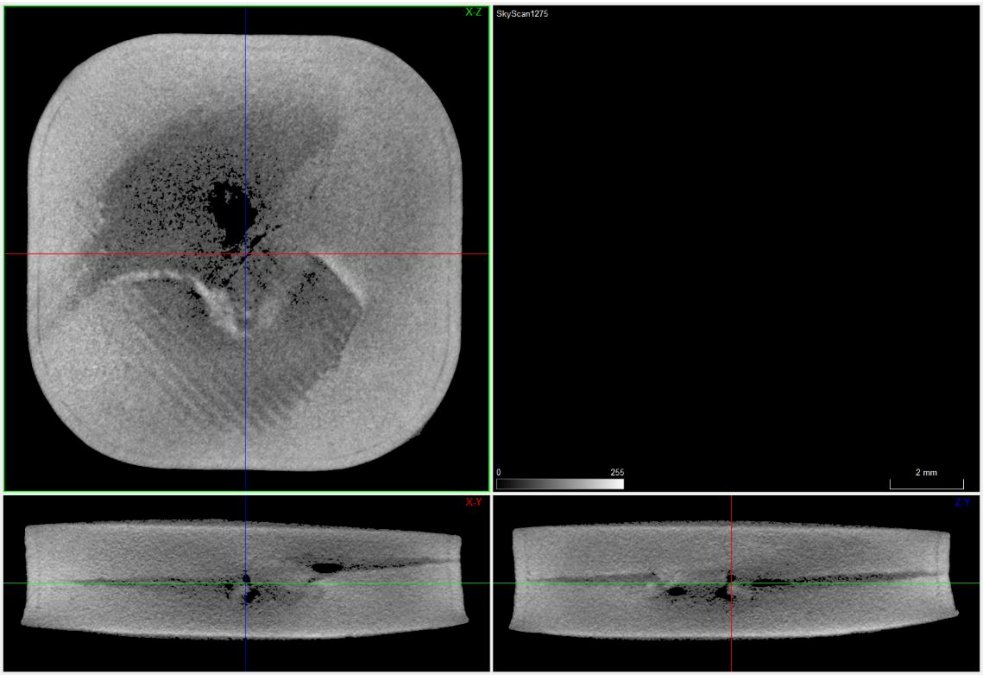

Figure 4.18. μCT images of 3D object 1.

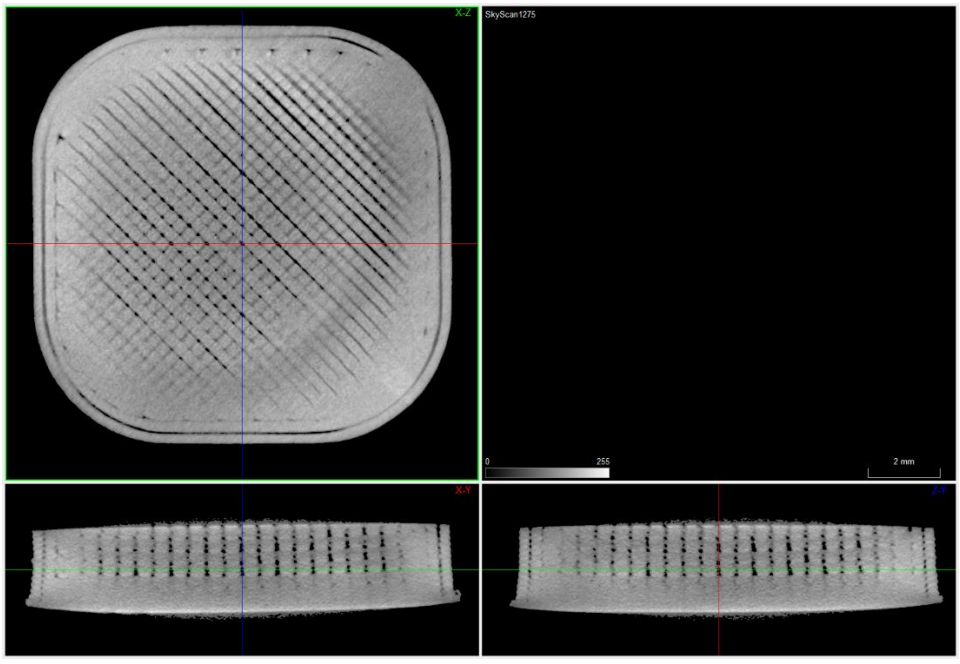

Figure 4.19. μCT images of 3D object 2.

Figure 4.20 and Figure 4.21 show a volumetric μCT view of 3D objects 1 and 2 highlighting the porosity (red colour). In agreement with the 3-plane μCT, it is possible to

observe that 3D object 1 porosity is essentially related to the occurrence of cracks. For 3D object 2, the porosity mostly follows the printing orientation.

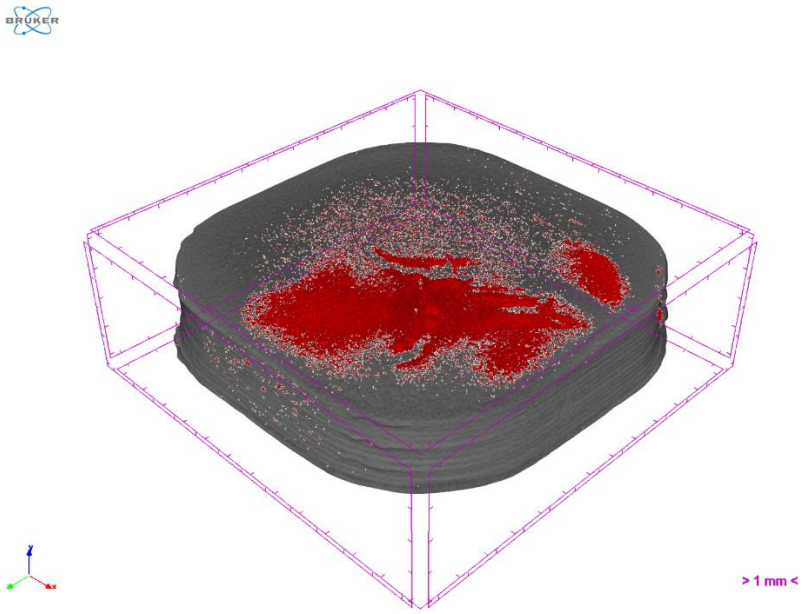

Figure 4.20. μCT image of 3D object 1 highlighting porosity.

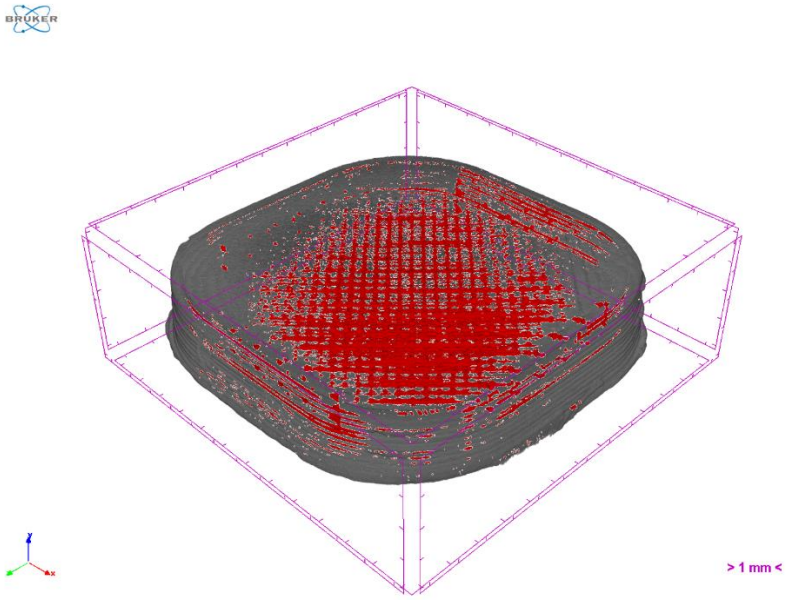

Figure 4.21. μCT image of 3D object 2 highlighting porosity.

4.6. Mechanical Characterization

4.6.1. Hardness and Young Modulus

The hardness and reduced Young modulus were calculated based on Oliver and Pharr's method [39]. A wrought manufactured (WM) 316L specimen and two 3D objects processed by MEX with different porosity levels (3D objects 1 and 2) were tested. The dedicated software calculates the reduced Young's modulus (E*) using the slope at the maximum load (unloading curve) and the projected area of contact. From the Poisson ratio (ν_I = 0,07) and Young modulus (E_I = 1050 GPa) of the diamond indenter, it is possible to obtain the Young Modulus (E) of the 3d object according to equation (4.3), once for steels the Poisson ratio (ν) can be assumed as 0.3.

$$\frac{1}{E^*} = \frac{1-\nu_I^2}{E_I} + \frac{1-\nu^2}{E} \tag{4.3}$$

The tested WM 316L presented a hardness of 2.9 ± 0.3 GPa which corresponds to about 295 HV and a Young modulus of 203 ± 31 GPa. An example of a loading/unloading curve of the WM material is shown in Figure 4.22

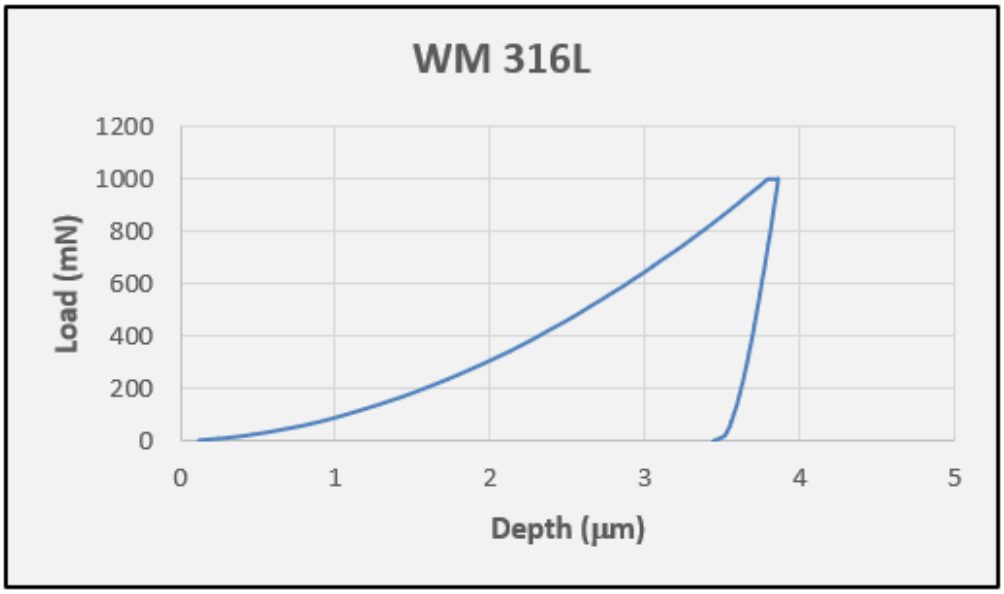

Figure 4.22. Load-Displacement curve for WM 316L.

3D object 1 presented a hardness of 1.7 ± 0.3 GPa, which corresponds to about 176 HV and 3D Object 2 had a hardness of 1.4 ± 0.2 GPa, which corresponds to about 148 HV. Examples of loading curves of 3D objects 1 and 2 are displayed in Figure 4.23 and Figure 4.24, respectively. Concerning the Young modulus, the obtained values for 3D objects 1 and 2 were very low and dispersive.

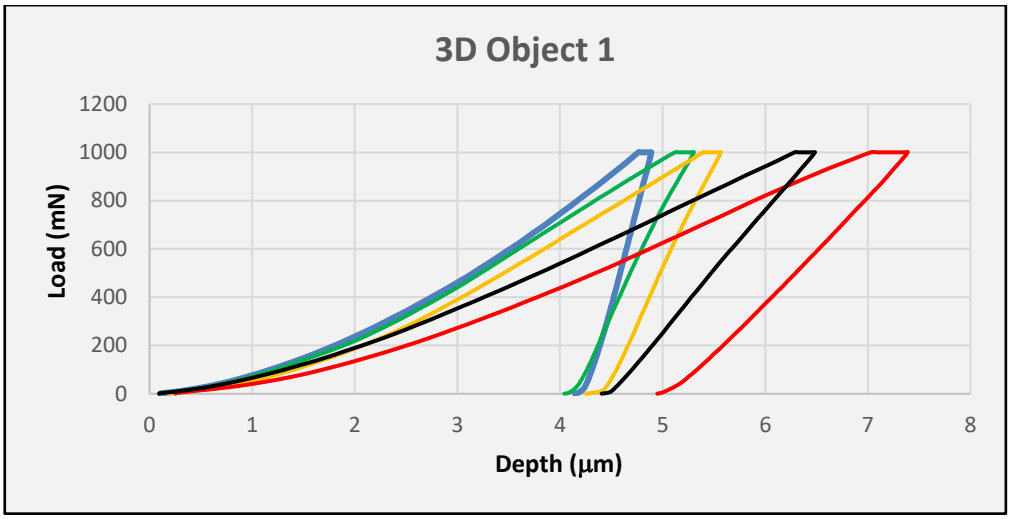

Figure 4.23. Load-Displacement curves for 3D object 1.

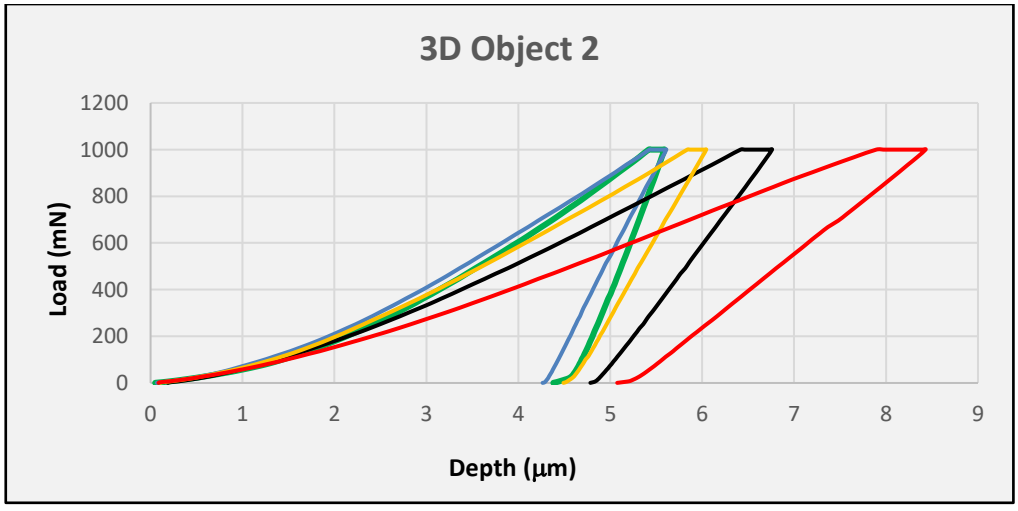

Figure 4.24. Load-Displacement curves for 3D Object 2.

Compared to the 316L processed by WM, the 3D objects present lower hardness and Young modulus due to their porosity. 3D object 1 presented higher hardness and elastic modulus than 3D object 2 since the last was more porous.

Figure 4.22 to Figure 4.24 assure that the more porous the specimens the deeper the indenter will reach, for the same material and load. Also, the depth of the affected volume

by the indentation (Figure 4.25) is considered to be at least 10 times the depth reached while applying the maximum load ($t \geq 10 \times h_{max}$). For 3D object 1 the affected depth would be until about $7{,}5 \times 10^{-6}\ m$ and for 3D object 2 until about $8{,}5 \times 10^{-6}\ m$, meaning that pores distributed below the indentation (within the presented range) influence the hardness and Young modulus values. In addition, the pore randomly distributed also contributes to the high standard deviation of the 3D objects.

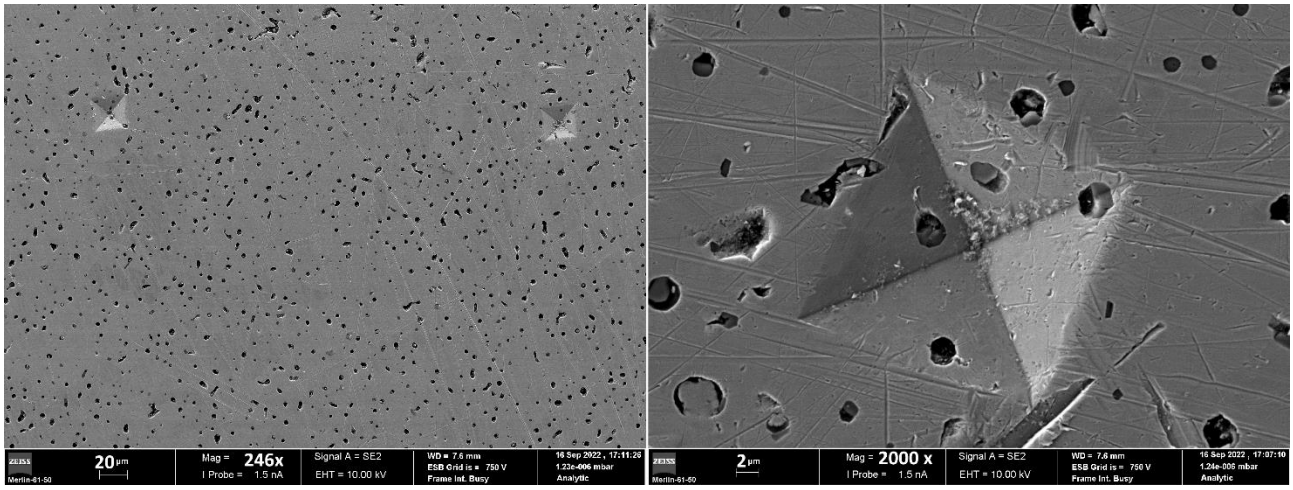

Figure 4.25. 3D object 1 depth-sensing indentations (SEM).

4.6.2. Microabrasion wear

3D objects 1 and 2 were investigated in a ball-cratering wear tester. For comparison purposes, a WM 316L specimen, theoretically without porosity, was also tested under the same conditions. The wear volume was calculated using equation (3.2) (Chapter 3).

Figure 4.26 highlights the diameter of the wear crater for the 3D object 1 after 200 rotations of the ball.

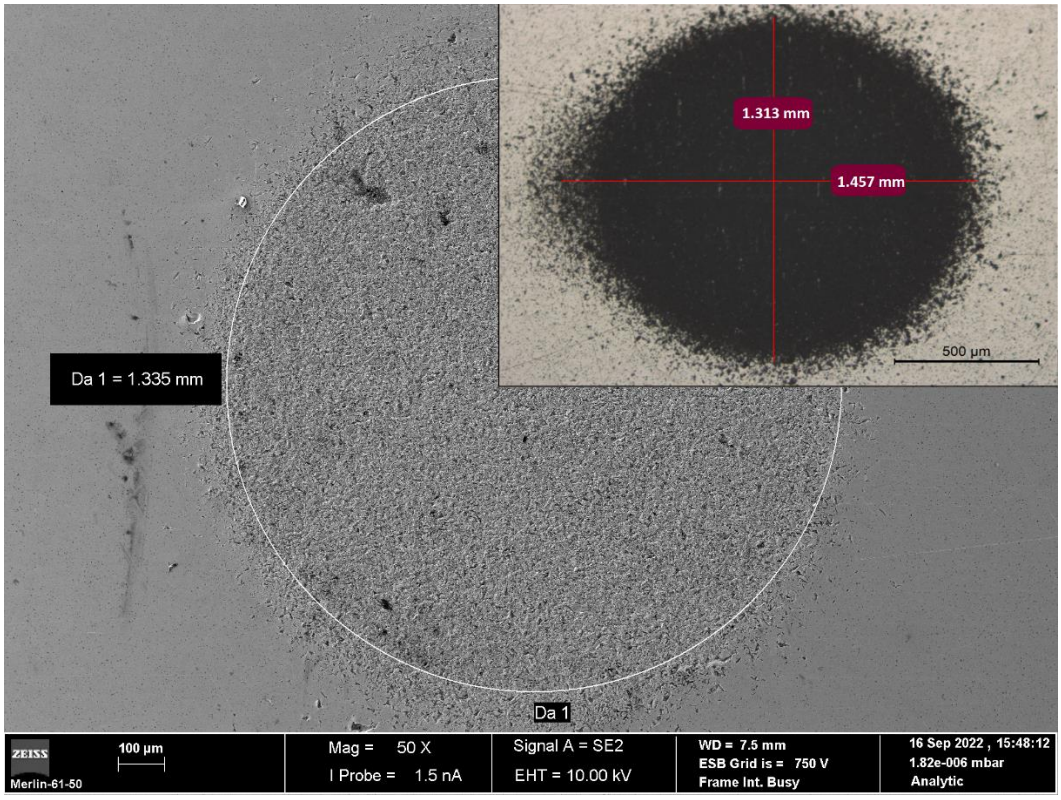

Figure 4.26. 3D object 1 crater diameters after 200 rotations of the ball (SEM and OM).

Figure 4.27 shows the variation of the wear volume function of the sliding distance times the normal load (kept constant at 0.2 N). From the figure, it is possible to notice a linear relationship between the sliding distance and the wear volume. A sliding distance increase corresponds to an increase in the wear volume of the 3D objects and WM. By establishing a linear relation that approaches the five measured points for each object of study and calculating their slope, it is possible to evaluate the wear coefficient through an adapted version of Archard's equation (4.4) where V is the wear volume, N is the normal load, L the sliding distance and k the specific wear rate [26], [40].

$$V = kLN \langle = \rangle k = \frac{V}{NL} \left(\frac{mm^3}{N \cdot m} \right) \tag{4.4}$$

The 3D object 2 was the one that presented the highest slope (0.32), which is expected due to its greater porosity and irregular surface (Figure 4.17 (right)). The WM presented the best wear resistance, i.e., the lowest k, being 36% more resistant than the 3D object 1 and 61% more resistant than the 3D object 2. The correlation coefficient values indicate a positive linear relationship, meaning that one variable tends to increase with the other.

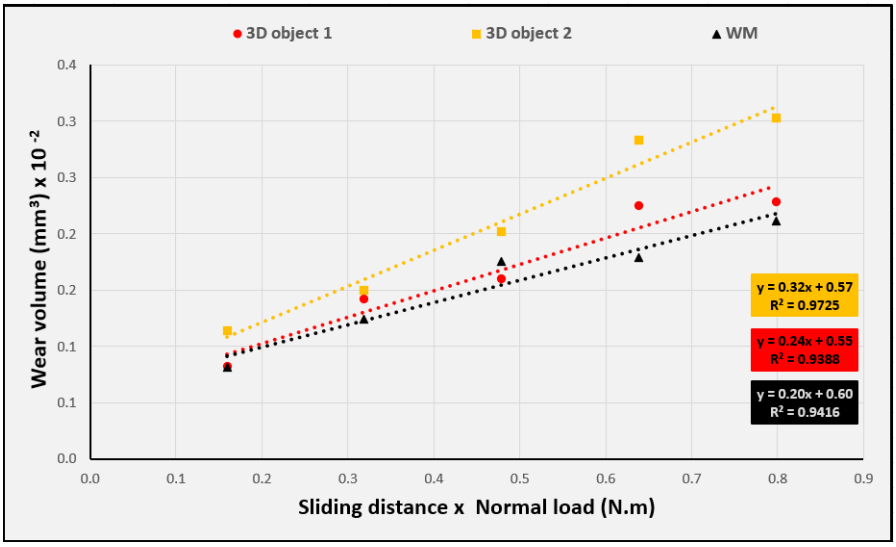

Figure 4.27. Wear volume function of the product sliding distance times x load for the three specimens.

Figure 4.28 shows the variation of the specific wear rate function of the sliding distance. It is possible to notice that by increasing the sliding distance the specific wear rate tends to present less deviation. The mainly descending variation of the specific wear coefficient shows no guarantee that a steady state was attained. Therefore, the results represent the evolution of the specific wear rate in the 3D objects and WM 316L under a transient regime, i.e., before reaching the steady state. Further investigation, increasing the sliding distance, must be conducted in order to firmly characterize the material under a steady state (for the available test condition). In addition, working under a steady state reduces statistical uncertainty.

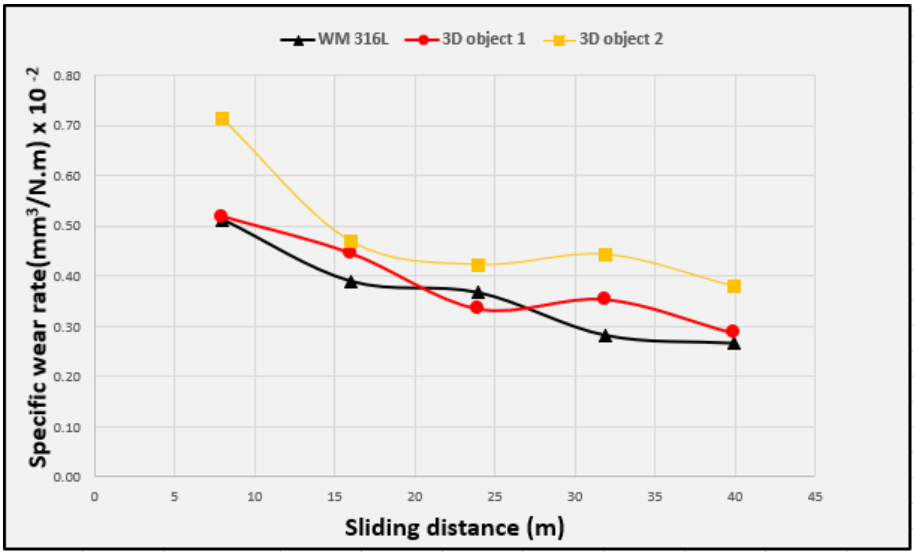

Figure 4.28. Specific wear rate function of the sliding distance for the three specimens.

Figure 4.29 to Figure 4.31 depict the wear scar profiles of the WM, 3D object 1, and 3D object 2 worn surfaces. Except for the 500 rotations on the 3D object 2, the depth and width of the wear scar increase with the increase of the number of rotations and, consequently, with the sliding distance. This behaviour is expected once the WM specimen and 3D objects are submitted to unfavourable conditions for larger periods.

A possible explanation for the fact that 3D object 2 presents a more pronounced wear scar after 400 rotations than 500 rotations, is that the surface part under 400 rotations has more printing lines visible, which can act as a defect that potentiates the abrasive wear effect (see Appendix B (B.4 (right)). In fact, mainly for 100 and 400 rotations, the wear profiles of MEX 2 specimens present deep valleys corresponding to the space between printing lines (Figure 4.31).

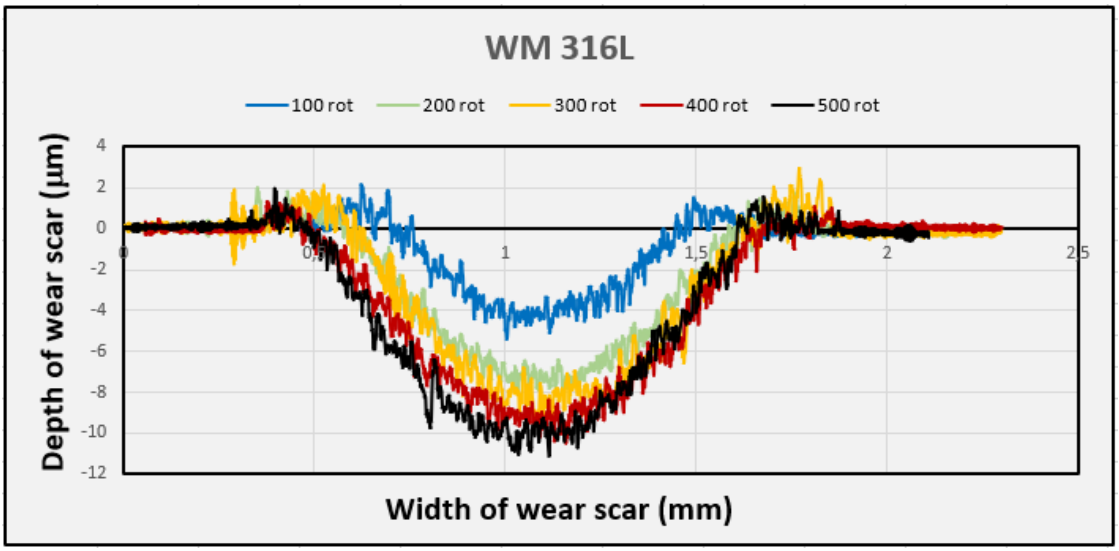

Figure 4.29. Wear scar profiles for the 316L WM for 100, 200, 300, 400, and 500 rotations of the ball.

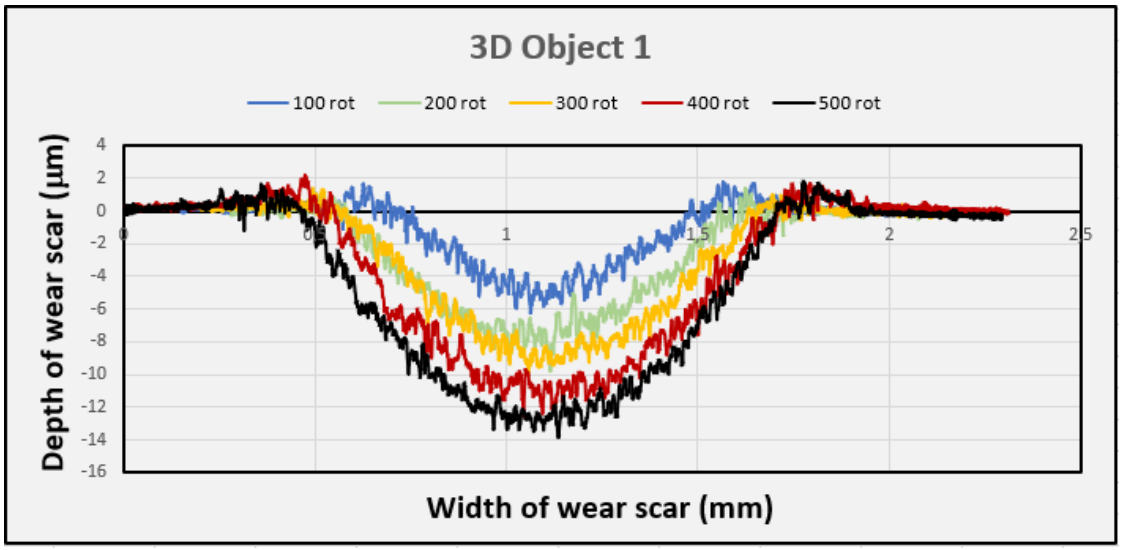

Figure 4.30. Wear scar profiles for the 3D object 1 for 100, 200, 300, 400, and 500 rotations of the ball.

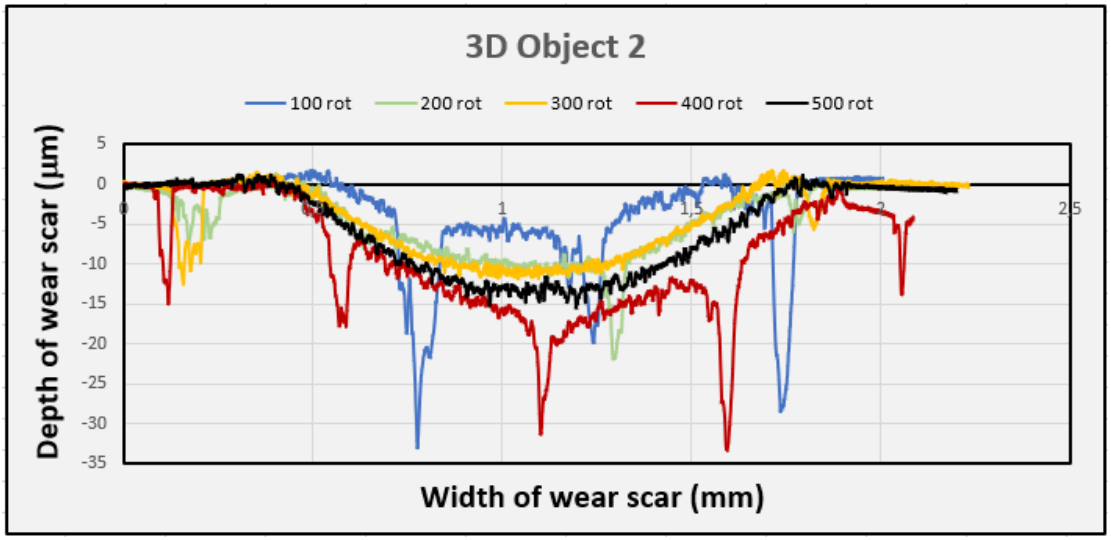

Figure 4.31. Wear scar profiles for the 3D object 2 specimen for 100, 200, 300, 400, and 500 rotations of the ball.

Figure 4.32 depicts the wear scar profiles of the worn surfaces after being exposed to 500 rotations. In agreement with the abrasive wear resistance coefficient, the WM presented the best performance under unfavourable conditions, and MEX 2 specimen the worst. This figure proves, once more, that porosity negatively contributes to wear resistance.

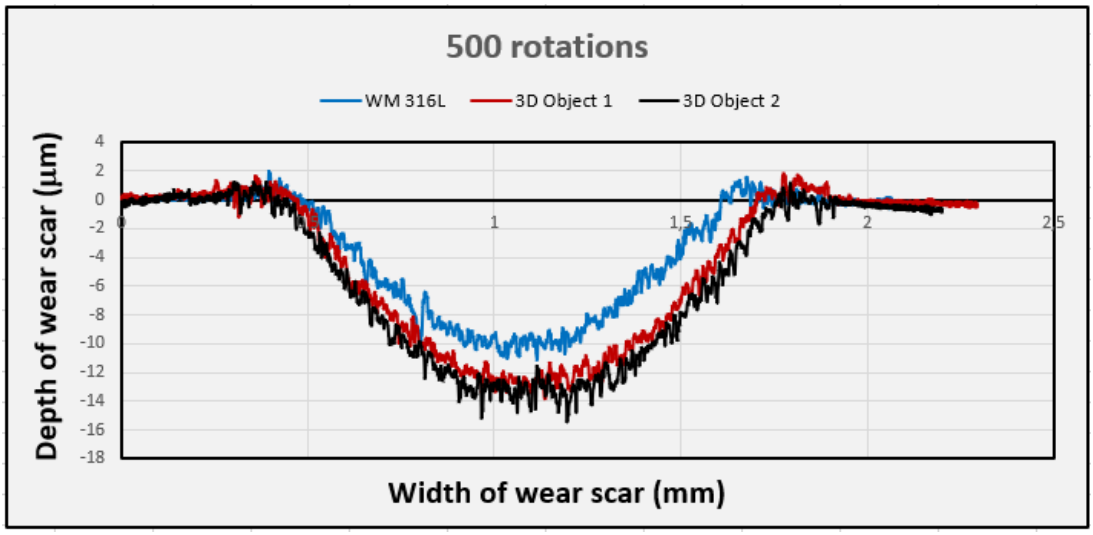

Figure 4.32. Wear scar profiles for the 316L WM, and 3D objects 1 and 2 at 500 rotations of the ball.

Overall, for the WM and 3D objects, the predominant abrasive wear mechanism was the rolling abrasion – three body rolling wear mechanism (Figure 4.33). The SEM (EDS) analysis also revealed some encrusted SiC particles resultant from the abrasive slurry. However, especially in the WM after 200 rotations and 3D object 2 after 300 rotations (2 out of 25 tests), some grooving effect was identified, as the SiC angular particles plastically deformed the surfaces (Figure 4.34).

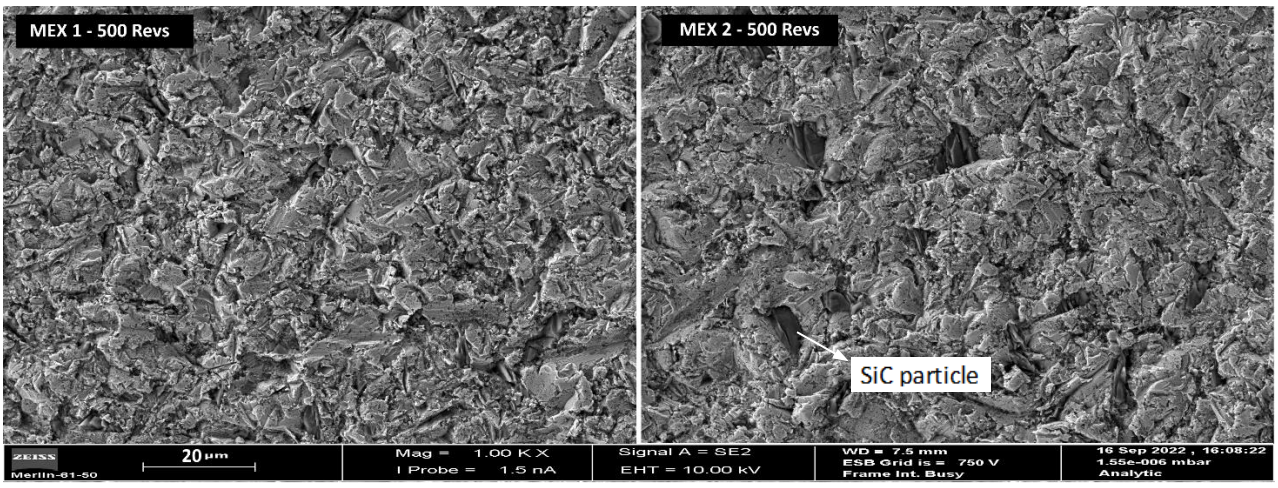

Figure 4.33. 3D object 1 and 2 micrographies of the crater highlighting rolling effect (SEM).

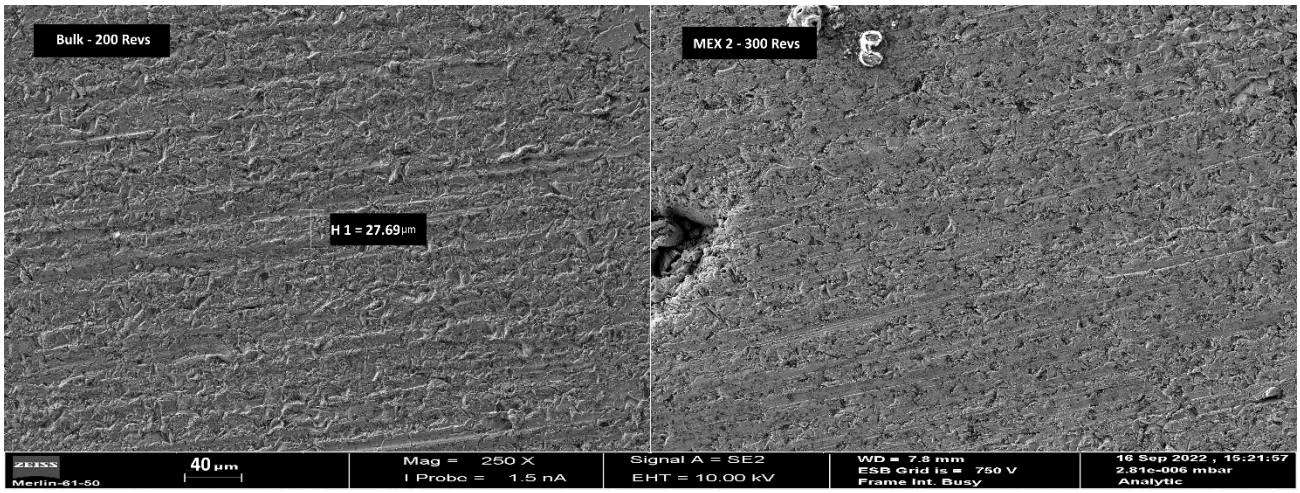

Figure 4.34. WM (200 rot.) and 3D object (300 rot.) micrographies inside the crater highlighting grooving effect (SEM).

Once 316L steel is low-hardness steel, considering the available conditions, not only was expected grooving to be more pronounced but also that grooving would occur mostly on 3D objects, as they presented lower hardness.

A relationship between hardness and abrasive wear mechanism or wear rate and abrasive wear mechanism could not be established as, overall, rolling abrasion was the only wear mechanism observed.

These results were obtained using the available conditions. Parameters optimization should be conducted with the aim of attaining suitable conditions to test MEX-obtained 316L 3D objects.

5. CONCLUSIONS

3D objects made from filaments with 60%vol. of 316L metallic powder were processed by MEX. The quality of 3D objects is function of their geometrical characteristics, particularly the thickness of the 3D object features. Debinding and sintering contribute to the consolidation of the brown, but not to correct the defects of shaping. 3D objects/features with thicknesses of 3 mm are the limit to contribute to low defects content. The inclusion of inside channels in the design of the 3D object without decreasing the structural properties required for its application would promote the efficiency of degassing and allow higher thicknesses.

The major challenge of AM is to obtain 3D objects with a density close to the bulk material. The initial stages of the process: feedstock and shaping parameters, were those that have the most impact on the quality of the 3D objects. One solution to overcome the enounced problem should be to submit the green specimens to Cold Isostatic Pressure (CIP) before the debinding and sintering cycle. This procedure may contribute to reduce the size of voids (due to the building strategy imposed) and eliminate eventual porosity.

Regarding the tribological performance, on the abrasive wear behaviour of the 3D objects produced by MEX, the WM presented an abrasive wear resistance 36% higher than the 3D object 1 and 61% higher than the 3D object 2. For the selected test conditions, rolling abrasion was the main abrasive wear mechanism observed. Moreover, ball-cratering tests revealed that a low porous, and defect-free surface tends to exhibit better resistance to abrasive wear, making it more likely to endure under adverse environments.

Finally, this study demonstrates that MEX can be a valid alternative to manufacture 316L stainless steel 3D objects with performance close to WM.

Future work

Based on the work developed, suggestions for future work can be as follows:

- Submitting green specimens to CIP with the aim of enhancing relative density.
- Develop new designs that include a system of degassing.
- Evaluate how pores can influence the abrasive wear mechanism.

- Optimise the ball-cratering parameters in order to study in detail the abrasive wear resistance.

BIBLIOGRAPHY

[1] V. Alcácer and V. Cruz-Machado, 'Scanning the Industry 4.0: A Literature Review on Technologies for Manufacturing Systems', *Engineering Science and Technology, an International Journal*, vol. 22, no. 3, pp. 899–919, Jun. 2019, doi: 10.1016/j.jestch.2019.01.006.

[2] 'ISO/ASTM 52900:2021(en), Additive manufacturing — General principles — Fundamentals and vocabulary'. https://www.iso.org/obp/ui/#iso:std:iso-astm:52900:ed-2:v1:en (accessed Sep. 07, 2022).

[3] F. Cerejo, D. Gatões, and M. T. Vieira, 'Optimization of metallic powder filaments for additive manufacturing extrusion (MEX)', *Int J Adv Manuf Technol*, vol. 115, no. 7–8, pp. 2449–2464, Aug. 2021, doi: 10.1007/s00170-021-07043-0.

[4] C. Suwanpreecha and A. Manonukul, 'A Review on Material Extrusion Additive Manufacturing of Metal and How It Compares with Metal Injection Moulding', *Metals*, vol. 12, no. 3, p. 429, Feb. 2022, doi: 10.3390/met12030429.

[5] M. Carminati, M. Quarto, G. D'Urso, C. Giardini, and G. Maccarini, 'Mechanical Characterization of AISI 316L Samples Printed Using Material Extrusion', *Applied Sciences*, vol. 12, no. 3, p. 1433, Jan. 2022, doi: 10.3390/app12031433.

[6] H. Ramazani and A. Kami, 'Metal FDM, a new extrusion-based additive manufacturing technology for manufacturing of metallic parts: a review', *Prog Addit Manuf*, Jan. 2022, doi: 10.1007/s40964-021-00250-x.

[7] M. Sadaf, M. Bragaglia, and F. Nanni, 'A simple route for additive manufacturing of 316L stainless steel via Fused Filament Fabrication', *Journal of Manufacturing Processes*, vol. 67, pp. 141–150, Jul. 2021, doi: 10.1016/j.jmapro.2021.04.055.

[8] A. S. Baskoro, S. Supriadi, and Dharmanto, 'Review on Plasma Atomizer Technology for Metal Powder', *MATEC Web Conf.*, vol. 269, p. 05004, 2019, doi: 10.1051/matecconf/201926905004.

[9] F. M. Barreiros and M. T. Vieira, 'PIM of non-conventional particles', *Ceramics International*, vol. 32, no. 3, pp. 297–302, Jan. 2006, doi: 10.1016/j.ceramint.2005.03.006.

[10] P. Singh, V. K. Balla, A. Gokce, S. V. Atre, and K. H. Kate, 'Additive manufacturing of Ti-6Al-4V alloy by metal fused filament fabrication (MF3): producing parts comparable to that of metal injection molding', *Prog Addit Manuf*, vol. 6, no. 4, pp. 593–606, Dec. 2021, doi: 10.1007/s40964-021-00167-5.

[11] X. Kan, D. Yang, Z. Zhao, and J. Sun, '316L FFF binder development and debinding optimization', *Mater. Res. Express*, vol. 8, no. 11, p. 116515, Nov. 2021, doi: 10.1088/2053-1591/ac3b15.

[12] M. Quarto, M. Carminati, and G. D'Urso, 'Density and shrinkage evaluation of AISI 316L parts printed via FDM process', *Materials and Manufacturing Processes*, vol. 36, no. 13, pp. 1535–1543, Oct. 2021, doi: 10.1080/10426914.2021.1905830.

[13] 'AISI 316L Stainless Steel Properties, Composition, Tensile Yield Strength'. https://www.theworldmaterial.com/aisi-316l-stainless-steel/ (accessed Jun. 27, 2022).

[14] Y. Wang, L. Zhang, X. Li, and Z. Yan, 'On hot isostatic pressing sintering of fused filament fabricated 316L stainless steel – Evaluation of microstructure, porosity, and

tensile properties', *Materials Letters*, vol. 296, p. 129854, Aug. 2021, doi: 10.1016/j.matlet.2021.129854.
[15] C. Suwanpreecha, P. Seensattayawong, V. Vadhanakovint, and A. Manonukul, 'Influence of Specimen Layout on 17-4PH (AISI 630) Alloys Fabricated by Low-Cost Additive Manufacturing', *Metall Mater Trans A*, vol. 52, no. 5, pp. 1999–2009, May 2021, doi: 10.1007/s11661-021-06211-x.
[16] M. Dular, T. Požar, J. Zevnik, and R. Petkovšek, 'High speed observation of damage created by a collapse of a single cavitation bubble', *Wear*, vol. 418–419, pp. 13–23, Jan. 2019, doi: 10.1016/j.wear.2018.11.004.
[17] C. Hardes, F. Pöhl, A. Röttger, M. Thiele, W. Theisen, and C. Esen, 'Cavitation erosion resistance of 316L austenitic steel processed by selective laser melting (SLM)', *Additive Manufacturing*, vol. 29, p. 100786, Oct. 2019, doi: 10.1016/j.addma.2019.100786.
[18] D. B. Pinto, 'Estudo da cavitação-erosão de materiais obtidos por sinterização', p. 58.
[19] 'Standard Test Method for Cavitation Erosion Using Vibratory Apparatus'. https://www.astm.org/g0032-03.html (accessed Sep. 07, 2022).
[20] H. Ding, Q. Tang, Y. Zhu, C. Zhang, and H. Yang, 'Cavitation erosion resistance of 316L stainless steel fabricated using selective laser melting', *Friction*, vol. 9, no. 6, pp. 1580–1598, Dec. 2021, doi: 10.1007/s40544-020-0443-7.
[21] M. Hauer *et al.*, 'Process Selection for the Fabrication of Cavitation Erosion-Resistant Bronze Coatings by Thermal and Kinetic Spraying in Maritime Applications', *J Therm Spray Tech*, vol. 30, no. 5, pp. 1310–1328, Jun. 2021, doi: 10.1007/s11666-021-01206-x.
[22] 'Standard Test Method for Conducting Wet Sand/Rubber Wheel Abrasion Tests'. https://www.astm.org/g0105-20.html (accessed Sep. 17, 2022).
[23] Y. Huang *et al.*, 'Microstructure and wear properties of selective laser melting 316L', *Materials Chemistry and Physics*, vol. 254, p. 123487, Nov. 2020, doi: 10.1016/j.matchemphys.2020.123487.
[24] F. Bartolomeu *et al.*, '316L stainless steel mechanical and tribological behavior—A comparison between selective laser melting, hot pressing and conventional casting', *Additive Manufacturing*, vol. 16, pp. 81–89, Aug. 2017, doi: 10.1016/j.addma.2017.05.007.
[25] H. Li, M. Ramezani, M. Li, C. Ma, and J. Wang, 'Tribological performance of selective laser melted 316L stainless steel', *Tribology International*, vol. 128, pp. 121–129, Dec. 2018, doi: 10.1016/j.triboint.2018.07.021.
[26] L. M. Vilhena, C. M. Fernandes, E. Soares, J. Sacramento, A. M. R. Senos, and A. Ramalho, 'Abrasive wear resistance of WC–Co and WC–AISI 304 composites by ball-cratering method', *Wear*, vol. 346–347, pp. 99–107, Jan. 2016, doi: 10.1016/j.wear.2015.11.005.
[27] M. G. Gee *et al.*, 'Progress towards standardisation of ball cratering', *Wear*, vol. 255, no. 1–6, pp. 1–13, Aug. 2003, doi: 10.1016/S0043-1648(03)00091-7.
[28] F. M. Barreiros and M. T. Vieira, 'Powder Injection Moulding to Recover Slate Wastes', *KEM*, vol. 230–232, pp. 247–250, Oct. 2002, doi: 10.4028/www.scientific.net/KEM.230-232.247.

[29] M.-S. Huang and H.-C. Hsu, ‘Effect of backbone polymer on properties of 316L stainless steel MIM compact’, *Journal of Materials Processing Technology*, vol. 209, no. 15, pp. 5527–5535, Aug. 2009, doi: 10.1016/j.jmatprotec.2009.05.011.
[30] M.-W. Wu, Z.-K. Huang, C.-F. Tseng, and K.-S. Hwang, ‘Microstructures, mechanical properties, and fracture behaviors of metal-injection molded 17-4PH stainless steel’, *Met. Mater. Int.*, vol. 21, no. 3, pp. 531–537, May 2015, doi: 10.1007/s12540-015-4369-y.
[31] O. M. Ferri, T. Ebel, and R. Bormann, ‘Influence of surface quality and porosity on fatigue behaviour of Ti–6Al–4V components processed by MIM’, *Materials Science and Engineering: A*, vol. 527, no. 7–8, pp. 1800–1805, Mar. 2010, doi: 10.1016/j.msea.2009.11.007.
[32] H. Gong, D. Snelling, K. Kardel, and A. Carrano, ‘Comparison of Stainless Steel 316L Parts Made by FDM- and SLM-Based Additive Manufacturing Processes’, *JOM*, vol. 71, no. 3, pp. 880–885, Mar. 2019, doi: 10.1007/s11837-018-3207-3.
[33] C. Burkhardt, P. Freigassner, O. Weber, P. Imgrund, and S. Hampel, *World PM2016 -AM -Deposition Technologies Fused Filament Fabrication (FFF) of 316L Green Parts for the MIM process*. 2021.
[34] J. Gonzalez-Gutierrez, D. Godec, C. Kukla, T. Schlauf, C. Burkhardt, and C. Holzer, *SHAPING, DEBINDING AND SINTERING OF STEEL COMPONENTS VIA FUSED FILAMENT FABRICATION*. 2017.
[35] J. Gonzalez-Gutierrez, S. Cano Cano, S. Schuschnigg, C. Holzer, and C. Kukla, *Highly-filled Polymers for Fused Filament Fabrication*. 2018.
[36] M. Á. Caminero, A. Romero, J. M. Chacón, P. J. Núñez, E. García-Plaza, and G. P. Rodríguez, ‘Additive manufacturing of 316L stainless-steel structures using fused filament fabrication technology: mechanical and geometric properties’, *Rapid Prototyping Journal*, vol. 27, no. 3, pp. 583–591, Jan. 2021, doi: 10.1108/RPJ-06-2020-0120.
[37] Y. Tao *et al.*, ‘A review on voids of 3D printed parts by fused filament fabrication’, *Journal of Materials Research and Technology*, vol. 15, pp. 4860–4879, Nov. 2021, doi: 10.1016/j.jmrt.2021.10.108.
[38] J. Safka, M. Ackermann, J. Machacek, M. Seidl, F. Vele, and V. Truxova, ‘FABRICATION PROCESS AND BASIC MATERIAL PROPERTIES OF THE BASF ULTRAFUSE 316LX MATERIAL’, *MM SJ*, vol. 2020, no. 5, pp. 4216–4222, Dec. 2020, doi: 10.17973/MMSJ.2020_12_2020071.
[39] W. C. Oliver and G. M. Pharr, ‘Measurement of hardness and elastic modulus by instrumented indentation: Advances in understanding and refinements to methodology’, *J. Mater. Res.*, vol. 19, no. 1, p. 18, 2004.
[40] A. Ramalho, ‘A reliability model for friction and wear experimental data’, *Wear*, vol. 269, no. 3–4, pp. 213–223, Jun. 2010, doi: 10.1016/j.wear.2010.03.023.

APPENDIX A

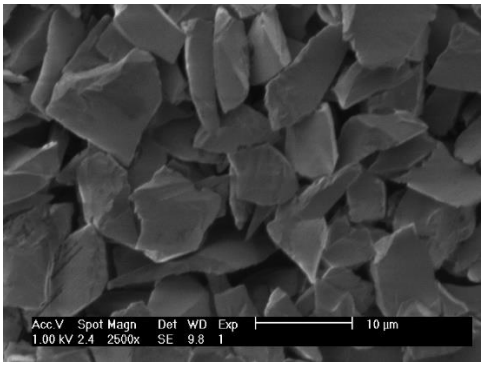

Figure A.1. Angular SiC particles (SEM).

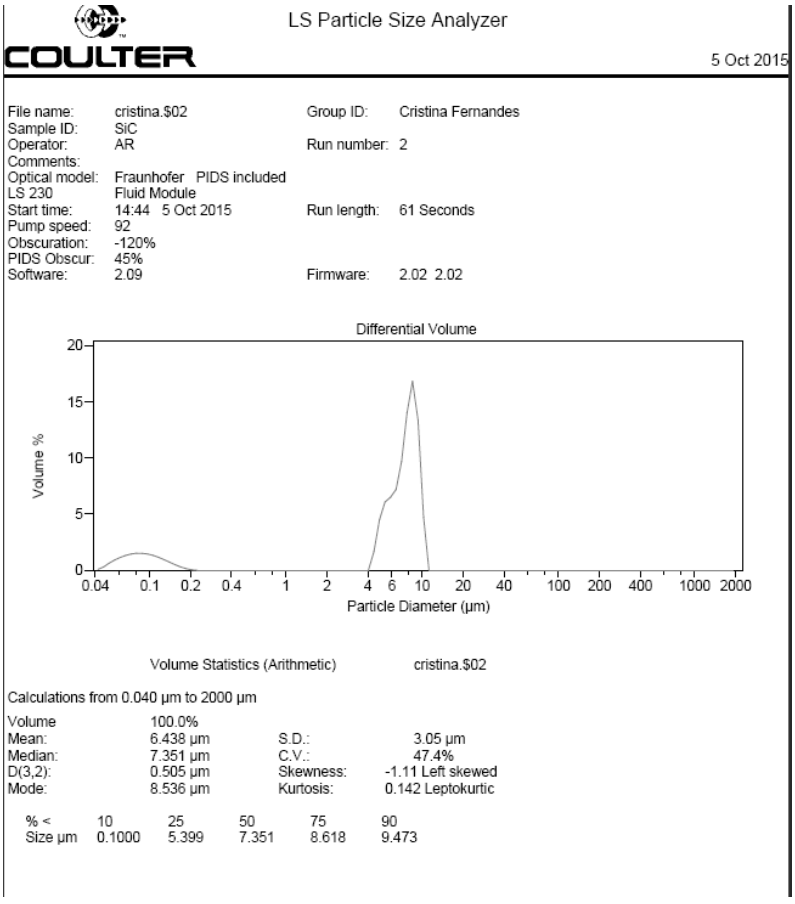

Figure A.2. SiC particles data highlighting particle size distribution.

APPENDIX B

Figure B.1. Plastograph Mixer (left) Maschinenbau Mil (right)**.**

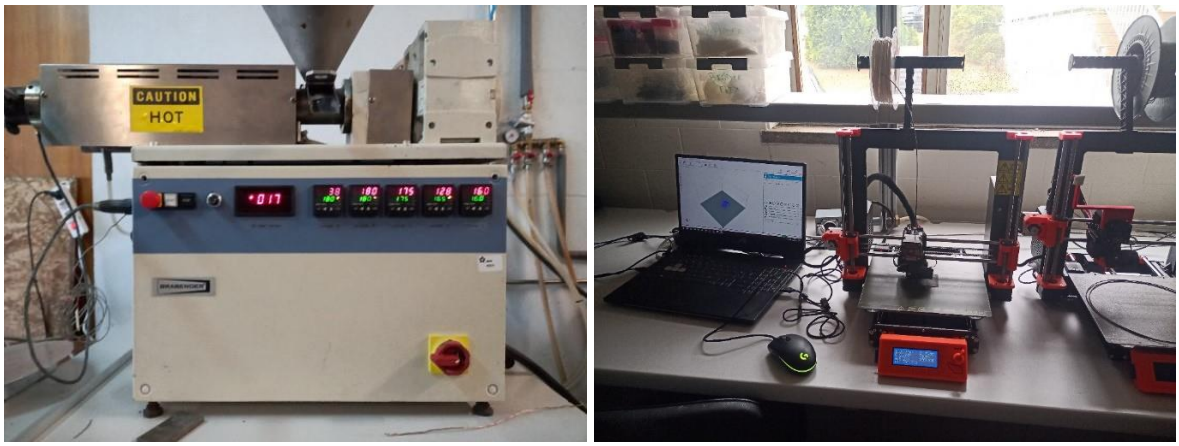

Figure B.2. Plastograph Single Screw Extruder (left) Prusa MK3s Printer (right).

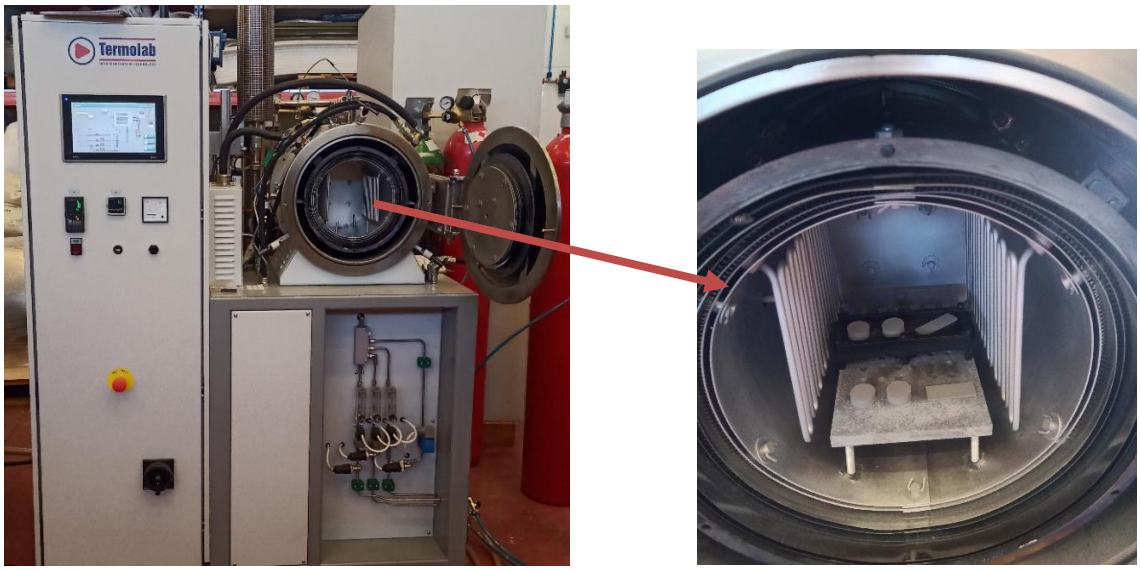

Figure B.3. Debinding and Sintering oven.

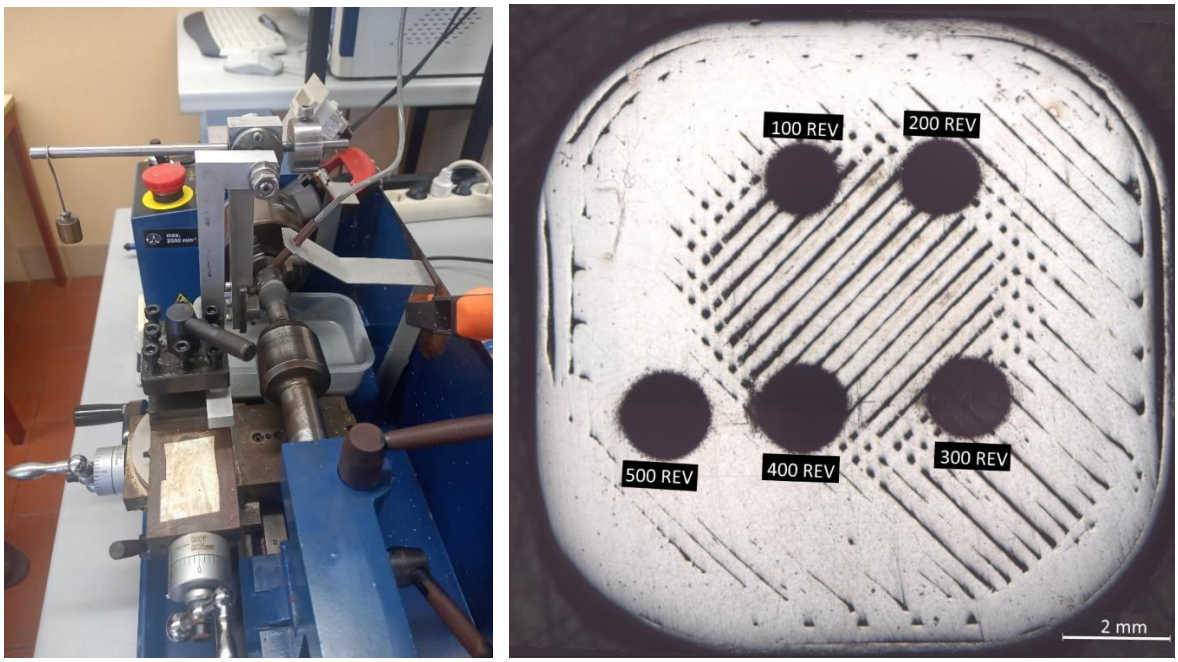

Figure B.4. Ball-cratering apparatus(left) 3D object 2 after ball-cratering (3 mm) (OM) (right).